Effect of Nanoporosity on the Selectivity of Copper Electrocatalysts for CO_2 Reduction

Master thesis

by

Qiaohui Lian

to obtain the degree of Master of Science at the Delft University of Technology,
to be defended publicly on September 23, 2025

Student number:	5843901	
Supervisors:	Dr. P. Taheri	TU Delft
	Dr. Y. Ma	TU Delft
	MSc. E. Best	TU Delft
Thesis committee:	Dr. P. Taheri	TU Delft
	Dr. Y. Ma	TU Delft
	Dr. S. Abrahami	TU Delft
	MSc. E. Best	TU Delft

Abstract

The conversion and utilization of CO_2 has attracted considerable research attention over the past few decades, as it not only contributes to emission reduction but also promotes more sustainable energy development. One promising approach for converting CO_2 into valuable products is the electrocatalytic CO_2 reduction (ECR) technology. In this mechanism, copper is widely recognized as an effective catalyst for reducing CO_2 into hydrocarbons such as methane and ethylene. To improve the catalytic performance, it is essential to investigate factors that influencing product selectivity. In this study, the effect of nanoporosity of copper powder on product selectivity was investigated. Porous copper powders were synthesized via a novel technique termed Intraparticle Expansion, which generates porous Cu by thermally reducing copper oxide in a simple and cost-effective manner through controlled reduction time and temperature. Electrochemical experiments were conducted using a gas diffusion electrode (GDE) flow cell. The catalytic performance of the reduced powders was compared with that of the initial CuO powder. Surface morphology was characterized using Scanning Electron Microscopy (SEM), while the intrinsic surface area and electrochemical surface area (ECSA) were evaluated by the Brunauer–Emmett–Teller (BET) method and Electrochemical Impedance Spectroscopy (EIS), respectively. Catalytic activity and stability were assessed via Linear Sweep Voltammetry (LSV) and Chronoamperometry (CA), and product distribution was analyzed using Gas Chromatography (GC) and High-Performance Liquid Chromatography (HPLC). Based on these results, nanoporosity was found to significantly influence the selectivity of specific products. The porous Cu samples exhibit higher faradaic efficiency toward C_2 products non-porous CuO at both -1.2 V and -2.5 V (vs. Ag/AgCl). Nevertheless, further optimization and more extensive experiments are required to fully validate these findings.

Acknowledgements

Over the course of my research journey, I have received generous support from many people, and I feel very fortunate to have had the opportunity to collaborate with all of you, to whom I would like to express my sincere gratitude.

First and foremost, I would like to thank my two supervisors. Prof. Peyman, who has been a guiding light in my research, helping me to develop my own understanding of this field, and for his contributions to the initial idea of this work and invaluable guidance in electrochemistry. Prof. Yan, who has taught me many essential aspects of scientific thinking, and whose careful supervision and insightful advice on material synthesis broadened my understanding of interdisciplinary collaboration between materials science and electrochemistry.

I am also very grateful to Prasaanth, Prasad, and Khaterah for their help and suggestions in material characterization and product analysis, guiding me in the use of instruments and generously spending time assisting with instrument maintenance. My thanks also go to Hans, Agnieszka, and Larine for their assistance in material synthesis, electrochemical experiments, and BET measurements. I would also like to thank many others who are not mentioned here individually, the combined efforts of all of you greatly contributed to the completion of this work.

I would like to give special thanks to my daily supervisor, Elsa, for her constant support. Thank you for patiently listening, helping me to reach out to others when challenges arose, and supporting me not only in research but also in maintaining my well-being.

Lastly, I would like to express my heartfelt gratitude to my family and friends for their continuous financial and emotional support, which gave me the courage and perseverance to complete this work. Without their unwavering encouragement, this thesis would not have been possible. Finally, I would also like to acknowledge myself, for the efforts, resilience, and dedication that carried me through moments of doubt and difficulty, and for the determination to continue moving forward on this journey.

Qiaohui Lian
Delft, September 2025

Contents

List of Figures

List of Tables

Nomenclature

Abbreviation	Definition
AERO	Additive Expansion by the Reduction of Oxides
BET	Brunauer–Emmett–Teller
BJH	Barrett-Joyner-Halenda
CA	Chronoamperometry
CPE	Constant Phase Element
CO_2RR	Carbon Dioxide Reduction Reaction
DFT	Density Functional Theory
ECSA	Electrochemical Surface Area
ECR	Electrocatalytic CO_2 Reduction
EDL	Electrical Double Layer
EIS	Electrochemical Impedance Spectroscopy
FE	Faradaic Efficiency
FID	Flame Ionization Detector
GDE	Gas Diffusion Electrode
GC	Gas Chromatography
HPLC	High-Performance Liquid Chromatography
LSV	Linear Sweep Voltammetry
MOFs	Metal–organic Frameworks
OCP	Open Circuit Potential
OD-Cu	Oxide-derived Copper
ORR	Oxygen Reduction Reaction
PEIS	Potentiostatic Electrochemical Impedance Spectroscopy
PTFE	Polytetrafluoroethylene
SAC	Single-atom catalyst
SEM	Scanning Electron Microscopy
TCD	Thermal Conductivity Detectors
TGA	Thermogravimetric analysis

1 Introduction

Energy is an inescapable topic in human activities. For a long time, the combustion of fossil fuels has been the primary method of energy generation. One of its most prominent by-products is carbon dioxide, which is also the main culprit behind the greenhouse effect. According to current emission data and professional forecasting models, global temperatures are projected to increase by 2.7 degrees by the end of this century[1, 2]. Therefore, mitigating CO_2 emissions is of critical importance. Several strategies have been proposed, including the adoption of alternative energy sources and efficiency improvements, CO_2 capture and sequestration, and CO_2 conversion and utilization[3]. Among these approaches, CO_2 conversion and utilization (Figure 1) has attracted considerable research attention, as it not only contributes to emission reduction but also achieve more sustainable energy development.

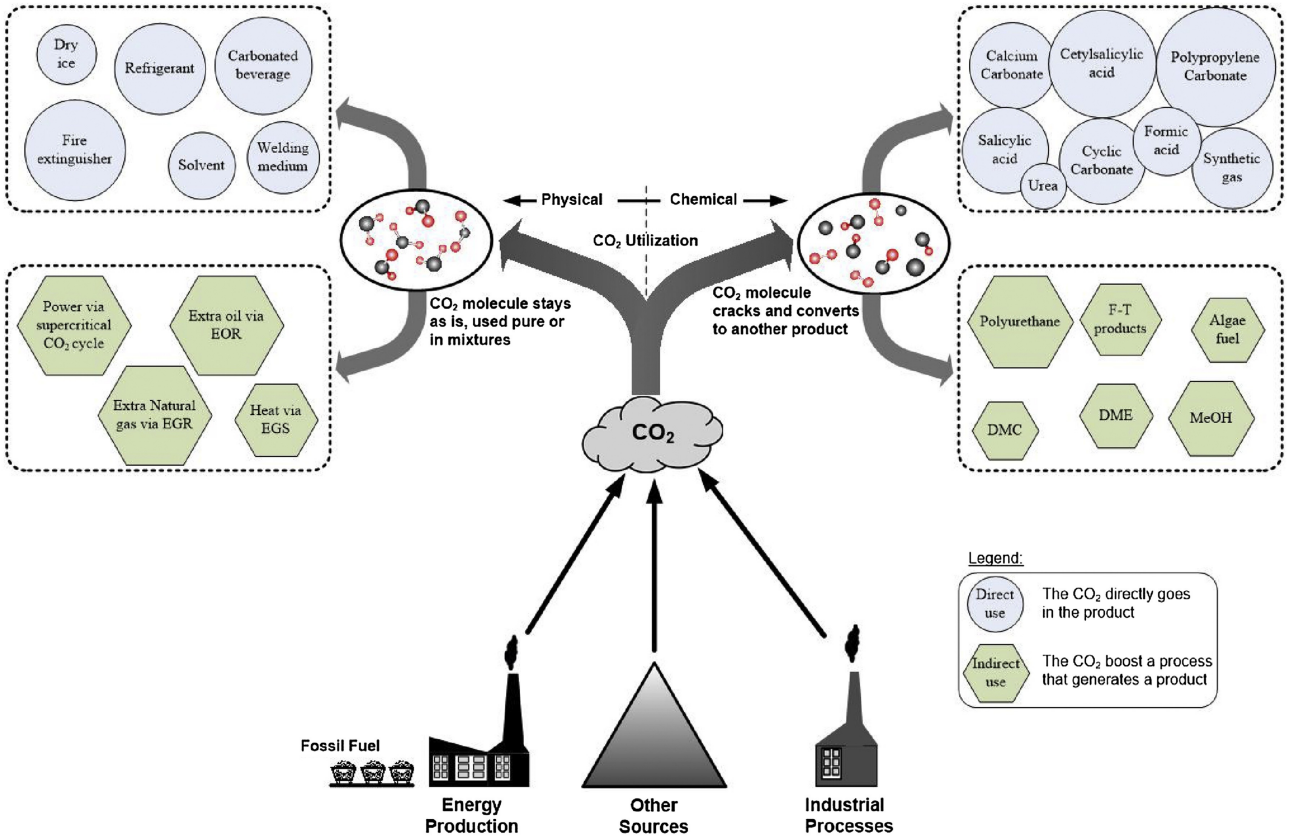

Figure 1: CO_2 utilization pathways[4].

Currently, various approaches through chemical process are available for CO_2 conversion, including electrochemical, thermal, biochemical, chemo-enzymatic, and photocatalytic techniques[5]. Among these, the electrochemical approach holds significant potential for CO_2 utilization and transformation, as it allows convenient storage of renewable electricity in a high-energy-density form[6].

Electrocatalytic CO_2 reduction (ECR) technology has garnered significant attention due to its favorable operational conditions, wide product distribution, and flexible energy sources. Currently, ECR is becoming increasingly mature, supported by a robust theoretical foundation derived from the oxygen reduction reaction (ORR) and hydrogen evolution reaction (HER)[7]. The working principle of ECR is illustrated in Figure 2, where the reaction typically occurs in a double chamber separated by an ion-exchange membrane, comprising an anode and a cathode. As shown, photo-anode and bio-anode can convert other energy sources into electrical energy, which will not be elaborated here[8, 9]. This project will primarily focus on the general anode. Usually, with an external potentiostat as the power supply, platinum (Pt) serves as the anode material. While the cathode material, functioning as the working electrode, facilitates CO_2 reduction.

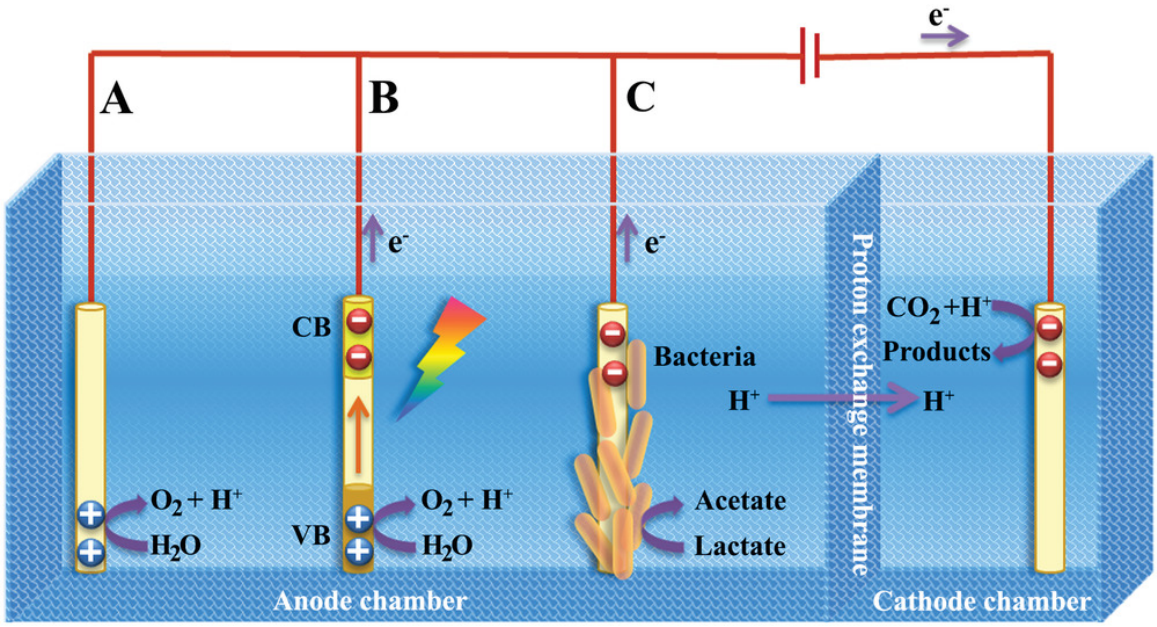

Figure 2: Various ECR systems using A) general anode, B) photo-anode, and C) bio-anode[7].

In energy conversion processes, catalysts often play a crucial role in reducing reaction barriers and enhancing reaction rates. In the reduction of carbon dioxide, the choice of catalyst is particularly critical, as it directly influences reaction efficiency, selectivity, and overall performance. Due to the inertness of CO_2, a key requirement for its reduction is the application of a high overpotential to overcome the energy barrier. However, excessively high overpotential can lead to hydrogen evolution as a competing reaction. This has created a demand for effective catalysts to accelerate ECR and supress HER[10]. Tailored electrocatalysts can stabilize key intermediates formed during the CO_2 reduction reaction (CO_2RR), thereby lowering the overpotential. The achievement of low overpotential and high selectivity is essential for optimizing CO_2 reduction, highlighting the critical role of electrocatalysts in this process[6, 7].

Electrocatalysts used for CO_2 reduction can be categorized into two types: homogeneous and heterogeneous. A homogeneous catalyst is a compound present in solution that diffuses to the electrode surface to facilitate electron transfer and capable of driving multiple proton-coupled reactions. This indirect electrolysis can prevent electrode passivation[11]. Transition-metal complexes with organic ligands are classic examples of homogeneous catalysts. Additionally, to limit catalysts usage, they can be immobilized on material surfaces, typically applied to conductive substrates, polymeric films, or carbon electrodes. Homogeneous catalysts help prevent CO_2 overbinding but may decompose and lead to suboptimal performance over long-term reactions[12]. In contrast, heterogeneous catalysts directly act as the cathode material to absorb electrons and combine with protons from the electrolyte to catalyze the CO_2 reduction at the electrode-electrolyte interface. A heterogeneous catalytic process typically consists of three stages: 1) the chemical adsorption of CO_2 onto the catalyst surface, 2) electron or proton transfer to facilitate the formation of CO or formate (C_1 product), and 3) product desorption from the catalyst surface through structural rearrangement, followed by diffusion into the electrolyte[13]. Compared to homogeneous catalysts, heterogeneous catalysts possess higher active surface areas, providing more sites for reaction. For example, heterogeneous catalysts such as nanostructured metals, alloys, and carbon-based materials enhance selectivity and reaction rates by increasing the density of accessible sites[7, 14, 15]. Among them, metal catalysts have garnered significant attention due to their structural simplicity, robustness, stability, and ease of synthesis. For CO_2 reduction, simpler C_1 products can be achieved near 100% Faradaic efficiency. However, for multi-carbon products, which are more valuable, improving their selectivity and efficiency remains a central focus of current research.

In particular, copper benefits from its electronic structure that endows it with moderate binding energy for *H and *CO, which contributes to reduce CO in aqueous electrolyte and generate C_{2+} species, making it highly valuable for CO_2 reduction studies[16, 17]. However, improvements are still required in terms of lowering the overpotential and achieving selectivity toward specific products. Moreover, the formation pathways of multi-carbon products on copper catalysts remain not fully understood, and catalyst durability continues to be a significant challenge, limiting their industrial-scale application[18, 19].

To overcome these challenges, several effective strategies have been developed to enhance catalytic performance while maintaining acceptable activity and efficiency. It is well-known that the surface engineering[20, 21, 22] and compositional modulation[23, 24, 25] can significantly influence CO_2RR by altering the local chemical environment through the adjustment of active sites and structural features, thereby affecting the overall catalytic process. In other words, product selectivity can be influenced by both the surface morphology and structural confinement, which can be further tuned by controlling the pore characteristics of the catalysts[26, 27].

In this project, the main objective is to investigate the effect of nanoporosity on product selectivity. To synthesize nanostructured porous copper, a novel method termed Intraparticle Expansion, or Additive Expansion by the Reduction of Oxides (AERO), was applied. This approach produces porous copper powder with varying degrees of porosity by reducing copper oxide under different controlled reduction time and temperature[28, 29]. The resulting porous powder was further processed into powder-based working electrodes and subjected to electrochemical experiments to evaluate its catalytic performance. The experimental techniques and results of these experiments are presented and discussed in detail in following sections. Finally, the key findings and potential improvements of the whole project are also summarized.

2 Theoretical Background

2.1 Fundamentals of CO_2 Electrochemical Reduction

As mentioned earlier, ECR is carried out under an applied potential, where the catalyst serves as the working electrode and is separated from the anode by an ion exchange membrane (Figure 3). Therefore, understanding the half-reaction processes of cathode involved is essential for investigating product selectivity.

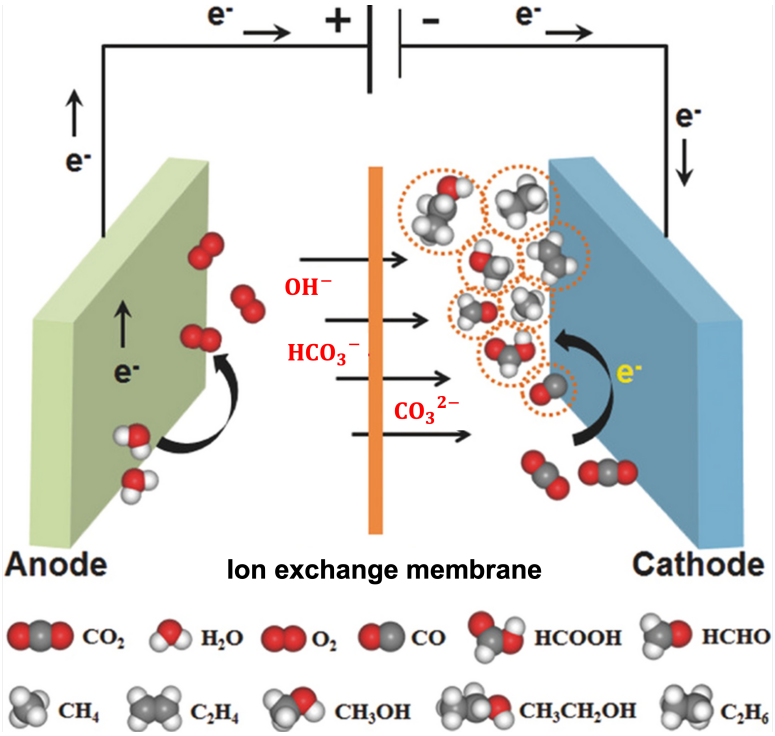

Figure 3: Process of CO_2RR and the possible products[30].

2.1.1 Thermodynamics of CO_2RR

CO_2 reduction is a multi-step reaction involving the transfer of multiple electrons, leading to a variety of products. For reduction reactions occurring in the liquid phase, CO_2 typically accepts electrons and protons to break C–O bonds and/or form C–H bonds, while interacting with active sites on the catalyst surface. These processes include adsorption and desorption steps, which generate specific intermediates or hydrocarbon products[18, 19]. Therefore, the standard electrochemical potentials (Table 1) of different products are critical for understanding the thermodynamic limitations of CO_2RR.

Table 1: Standard electrochemical potentials for CO_2 RR[18]

Products	**Reaction**	**E° (V) vs. SHE (pH 7)**
Carbon monoxide (CO)	$CO_2 + 2e^- + 2H^+ \rightarrow CO(g) + H_2O$	-0.53
Hydrogen (H_2)	$2e^- + 2H^+ \rightarrow H_2(g)$	-0.42
Formic acid (HCOOH)	$CO_2 + 2e^- + 2H^+ \rightarrow HCOOH(l) + H_2O$	-0.61
Formaldehyde (CH_2O)	$CO_2 + 4e^- + 4H^+ \rightarrow CH_2O(l) + H_2O$	-0.50
Methanol (CH_3OH)	$CO_2 + 6e^- + 6H^+ \rightarrow CH_3OH(l) + H_2O$	-0.39
Methane (CH_4)	$CO_2 + 8e^- + 8H^+ \rightarrow CH_4(g) + H_2O$	-0.25
Ethylene (C_2H_4)	$CO_2 + 12e^- + 12H^+ \rightarrow C_2H_4(g) + 4H_2O$	-0.38
Ethane (C_2H_6)	$CO_2 + 14e^- + 14H^+ \rightarrow C_2H_6(g) + 4H_2O$	-0.28

Interestingly, the standard potentials are not particularly high, and products such as methane and ethylene

exhibit more favorable potentials than hydrogen. However, the small differences among these standard potentials make it difficult to generate targeted products with high selectivity. Moreover, it is important to note that under practical conditions, the applied potentials are typically different from the standard values due to kinetic and environmental constraints. This leads to the introduction of the concept of overpotential. By tuning the reaction conditions and surface morphology of catalyst, the overpotential can be reduced[31].

2.1.2 Catalytic performance

Overpotential is one of the key indicators for evaluating catalytic performance, as it reflects the reaction energy barriers. The overpotential is defined as the absolute difference between the applied potential and the corresponding standard (or equilibrium) potential[31], as expressed in the following equation:

$$\eta = |E_{\mathrm{a}} - E^{\circ}| \tag{1}$$

where η is the overpotential, E_{a} is the applied potential (V), and E° is the standard (equilibrium) potential (V).

In practice, catalytic performance is often evaluated in terms of both activity and selectivity[32]. The activity is commonly represented by the measured current normalized to the electrochemical surface area (ECSA), which can be calculated as:

$$i = \frac{I_{\mathrm{recorded}}}{\mathrm{ECSA}} \tag{2}$$

where i is the current density (mA cm^{-2}), I_{recorded} is the measured current (mA), and ECSA is the electrochemical surface area (cm^2)[32].

Selectivity, is typically expressed in terms of the Faradaic efficiency (FE), which quantifies the fraction of the total current consumed to produce a specific product:

$$FE = \frac{n \cdot z \cdot F}{Q} \times 100\% \tag{3}$$

where z is the number of electrons transferred, n is the number of moles of the desired product, F is Faraday's constant (96 485 C mol^{-1}), and Q is the total charge passed during electrolysis[32].

In summary, an ideal catalyst for CO_2 reduction should exhibit a low overpotential, high activity, and high selectivity toward the desired products, which together define excellent catalytic performance.

2.2 State-of-art Copper-based Electrocatalysts

Copper catalysts in CO_2 reduction are capable of producing C_{2+} products due to their binding strength with key intermediates, which provides excellent sites for carbon-carbon coupling[15, 19]. To date, more than sixteen CO_2 reduction products have been reported[33]. The unique ability to generate high-value products has attracted considerable research interest in copper-based catalysts. Recent advancements of copper-based electrocatalysts for enhanced catalytic performance will be introduced in following sections.

2.2.1 Copper single-atom catalysts

Single-atom catalyst (SAC) exhibits uniform dispersion and nearly 100% atomic utilization due to the unique electronic structure of the atomic metal center. However, the unsaturated anchoring sites in SACs hinders C–C coupling, leading to the preferential formation of C_1 products[34]. This limitation can be addressed by introducing specific carriers. When SACs are connected to carriers via covalent or ionic bonds, the resulting metal-support interaction can modulate the d-state electronic structure of the metal centers. These interactions optimize catalytic performance by enhancing the adsorption and desorption of key intermediates[19]. Consequently, the choice of carrier plays a crucial role in selective formation of C_2 products in CO_2RR. Carbon-based materials, heteroatom-doped supports, and metal–organic frameworks (MOFs) are the most widely used carriers and have achieved remarkable progress in promoting the formation of multi-carbon products[23, 34]. Recent studies have increasingly focused on atomic Cu anchored onto various carriers, resulting in composite catalysts with superior performance. For example, Shen et al. developed a MOF-derived carbon-based catalyst, in which

MOF shells encapsulate copper active sites through charge-transfer interaction, thereby promoting uniform dispersion of the metal centers. This unique MOF-derived Cu–carbon composite achieved a Faradaic efficiency of 75.6% for C_2 products at a C_2 partial current density of 377.9 mA/cm^2[35]. Similarly, studies have shown that the catalytic performance of single-atom sites can be effectively tuned by modifying the local microenvironment when carbon is doped with nitrogen. A nitrogen-modified carbon-supported Cu nanoclusters has been reported to achieve an excellent C_2H_4 Faradaic efficiency of 61.4% with a current density of 208 mA/cm^2 at -1.05V(vs RHE)[36].

2.2.2 Cu-based bimetal catalysts

For Cu-based systems, the incoporated-alloyed metals adopt various atomic arrangements that significantly improve catalytic performance in CO2RR. To date, the combined metal elements include both precious(Au[37, 38], Ag[39, 40], Pb[41]) and non-precious(Zn[42, 43], Ni[44], Ti[45], Sn[46], Bi[47], Pd[48]). The interaction between the metals allows the d-band center of Cu shift to Fermi level. The resulting reconstruction of surfaces electrons modify catalytic performance by affecting the adsorption and activation of intermediates. For example, the Cu-Pd catalyst favors the formation of CH_4, Cu-Ni predominantly generate CH_3OH. As for Cu-Ag, CO is thermodynamically and kinetically favored[49]. Not only the type of alloyed metal but also its compositional ratio plays a critical role in tuning the product selectivity. Chen et al. designed a series of CuZn-based catalysts with varying Zn ratios to investigate their CO_2RR performance. They observed that the highest Faradaic efficiency for CO production (61%) was achieved at a Cu/Zn ratio of 1:9. However, the Faradaic efficiency of CH_4, $HCOO^-$, C_2H_5OH, and CH_3COO^- remained unchanged with the variation of Cu/Zn ratio. This outcome can be attributed to the Zn sites, which selectively promote *CO binding while suppressing *H adsorption. Therefore, the formation of C_2H_4 was outcompeted by CO generation. Furthermore, they reported that the incorporation of Ni inhibited hydrogen evolution, thereby enabling the catalyst to reach the CO Faradaic efficiency up to 80%[24]. Similarly, Su and co-workers evaluated the effect of Ag content in CuAg bimetallic catalysts and identified the optimal composition for enhanced catalytic performance. At a Cu/Ag ratio of 1:5, the abundant Ag component thermodynamically promotes C–C coupling, facilitating the formation of ethanol while suppressing H_2 and C_2H_4 production. A maximum Faradaic efficiency of 51.8% for C_2H_5OH was achieved at -1.0V(vs RHE)[25].

2.2.3 Oxide-derived Cu catalysts

Oxide-derived Cu (OD-Cu) catalysts have also attracted significant attention in CO2RR due to their unique surface properties. Several studies suggest that the oxidation state and structure play a critical role in determining both catalytic activity and selectivity. It has been reported that metastable sites (particularly undercoordinated sites) on OD-Cu surfaces enable strong interactions with CO. The CO binding strength on these sites is higher than that on low-index and stepped Cu facets, which is fundamental to the high CO_2 reduction activity of oxide-derived Cu[17, 50]. Compared to metallic Cu, OD-Cu demonstrates significantly enhanced selectivity toward ethylene and ethanol. In general, OD-Cu catalysts can be synthesized by chemical deposition or thermal treatment. By controlling parameters such as treating time, current density, PH and temperature, the surface morphology and structural characteristics can be effectively modulated to optimize the catalytic performance[51]. For instance, Li and Kanan et al. investigated the influence of copper oxide layer thickness on CO_2RR performance by varying the annealing temperature. Their results showed that a thicker Cu_2O film (≥ 3 μm) reduced the overpotential by approximately -0.5V compared to polycrystalline Cu and exhibited more stabale catalytic activity[52]. Wei and coworkers further elucidated the role of adsorbed hydroxyl species (OH_{ad}) on the surface of OD-Cu. By combining electrochemical reduction and thermal treatment, they successfully fabricated OD-Cu catalysts with sub-20 nm surface nanoparticles. Their study revealed that OH_{ad} promotes (1) the adsorption of low-frequency CO and C$\equiv$O species, and (2) the dimerization of CO intermediates. These effects were consistently observed in both H-type cells and electrolyte flow cells. However, an excessive concentration of OH_{ad} may lead to increased H_2 evolution. Under optimized conditions, this OD-Cu catalyst achieved stable C_2 product generation with a high selectivity of approximately 60% at a current density of 200 mA/cm^2 and a potential of -0.95V(vs RHE)[53].

2.2.4 Organic-derived Cu catalysts

Organic ligands can modify the surface properties of catalysts by modulating the electronic and steric environment around the active sites. The interaction between hydrophobic/hydrophilic functional groups and key

intermediates is crucial in tuning product selectivity[19, 54]. For example, incorporating hydrophobic trifluoromethyl (–CF_3) functional group onto Cu nanoparticles has been shown to enhance the formation of C_{2+} products. This surface modification leads to an increased *CO coverage and a reduced formation energy for the *COCOH intermediate, while also suppressing H_2O accessibility. These combined effects promote C–C coupling, leading to a high C_{2+} product Faradaic efficiency of 71.08% and an impressive partial current density of 355.4 mA/cm^2[55]. The introduction of quinone groups has also shown excellent performance in promoting the formation of C_2 products, particularly ethylene. Owing to their high CO_2 affinity, quinone groups can directly react with CO_2 to form carbonate adducts. This accelerates conversion of CO_2 to CO, resulting in high surface CO coverage, which in turn promotes C–C coupling. As a result, Li et al. reported a remarkable partial current density for ethylene of up to 325 mA/cm^2 in CO2/pure water coelectrolysis[56].

2.3 Effect of Nanoporosity

An effective approach to enhance their catalytic performance of copper-based materials is tuning the porosity. Nanostructured catalysts, with their increased exposed surface area, provide a larger number of active sites, thereby facilitating CO_2 RR. Moreover, the well-controlled microstructure of the catalyst can influence the transport and diffusion of reactants and intermediates, ultimately affecting product selectivity[26]. In particular, pore dimensions and distribution are critical factors that significantly impact the selectivity of CO_2RR products[57]. This section focuses on the effects of nanoscale microstructures during catalysis.

2.3.1 Confinement

In recent years, nanotechnology has been extensively applied in catalyst design. As expected, catalysts with nanoporous structures often exhibit superior catalytic performance compared to their conventional counterparts. Improvements in catalytic performance involves the enhanced catalytic activity and increased product selectivity. The steric confinement effect mainly regulates selectivity by influencing diffusion processes. Within interconnected porous networks, diffusion gradient generated by the pore structure manipulates the fluxes of reactants, intermediates, and products[58]. Additionally, cavity confinement induces diffusion retardation, which increases the residence time of key reaction intermediates, thereby affecting reaction pathways and selectivity[26]. For example, Yang et al. demonstrated that nanocavities helped to lock the local concentration of carbon intermediates, effectively masking the active CO_2RR surface and preventing the reduction of Cu^+ species. Their multihollow cuprous oxide catalyst achieved a Faradaic efficiency exceeding 75% for C_{2+} products at partial current densities above 250 mA/cm^2[59]. Similarly, Zhong et al. found that an increased local CO concentration resulting from the confinement effect in a core-shell Ag@Cu catalyst enhances C–C coupling, with the catalyst achieving a Faradaic efficiency of 73.7% for C_{2+} products at 300 mA/cm^2[60]. More recently, Kong and coworkers confirmed that spatial confinement-induced diffusion retardation positively influenced *CO concentration. Their porous carbon-supported Cu nanocluster electrocatalyst exhibited a Faradaic efficiency of approximately 74% for multi-carbon products under industrially relevant partial current densities[58]. Pan et al. fabricated bicontinuous porous CuO nanofibers featuring long-range mesochannels via microphase-separated block copolymers. Their density functional theory (DFT) calculations suggested that enhanced confinement promotes the adsorption of OH_{ad} and O_{ad} species, facilitating CO–CO dimerization and CO–CHO coupling. This special design achieved a C_2 Faradaic efficiency up to 74.7%, significantly outperforming catalysts with conventional short-range pores[61]. Moreover, hydrogen evolution can be suppressed by limiting the excess protons, which in turn favors CO_2 adsorption by preserving more active sites. For instance, Hall et al. demonstrated that the thickness of Au-IO thin films plays a crucial role in hydrogen suppression during CO_2 reduction[26].

2.3.2 Pore structure

Numerous studies have demonstrated a strong correlation between surface morphology and product selectivity. Active sites for C–C coupling, as well as reaction intermediates, tend to be retained within mesopores, thereby influencing catalytic performance[62, 63, 64, 65]. Sen et al. synthesized 3D hierarchical foamed porous Cu with pore diameters ranging from 20-50 μm, exhibiting dominant (111), (200), and (220) orientations. The observed pore diameter gradient was attributed to nanoscale dendritic structures surrounded by interconnected channels, which extended the retention time of reaction intermediates. This structural feature enableed the formation of multi-carbon products such as propylene. Moreover, they elucidated the interaction between critical concentration and the electrical double layer (EDL) to explain product selectivity. When the EDL thickness exceeds the pore volume, the pore's inner surface area becomes inaccessible. At minimum EDL thickness, nanoscale

pores lower the desorption energy of surface-bound intermediates, enhancing retention time for better catalytic performance[66]. Yang et al. further investigated the interaction mechanism between pore volume and the EDL and its effect on the product selectivity of Cu mesoporous electrodes. By comparing three types of Cu meshes with mesopores: 30nm width and 40nm depth, 30nm width and 70nm depth, and 300nm width and 40nm depth. They found that smaller and deeper pores led to an increased C_2 /C_1 product ratio. In addition, they highlighted the role of mass transport in the reaction process. At lower flow rates, EDL overlapped within the narrow and deep pores trapped reaction intermediates, extending their residence time and enhancing C–C coupling. As the flow rate increased, although the total current density also rose, the catalytic performance was diminished due to an intensified hydrogen evolution reaction [67].

The interaction of pores and confinement effect also plays a significant role in determining product selectivity. As previously mentioned, the confinement effect in a core–shell Ag@Cu catalyst enhanced C–C coupling. In this study, the researchers simultaneously emphasized the effect of pore size. By comparing porous Cu shells with average pore diameters of 2.8, 4.9, and 11.2 nm, they found that the 4.9 nm pores most effectively enhanced the local CO concentration, resulting in a Faradaic efficiency for C_{2+} products of 73.7%[60]. Another recent study demonstrated that the pore structure of the catalytic layer in a gas diffusion electrode can directly influence product selectivity by modulating the local electrolyte microenvironment. A highly porous catalyst layer enhanced the mass transport of alkaline ions, thereby maintaining a stable local supply of both H^+ and CO_2. As a result, the catalyst layer with higher porosity (80%, average pore size: 224.71nm) achieved a significantly higher C_2^+ Faradaic efficiency of 79.61%, compared to a less porous layer (porosity: 68%, average pore size: 263.62nm), which exhibitd only 38.20%[68]. A very recent study further investigated the relationship between porosity and catalytic performance. Tsai and his colleagues compared the CO_2 reduction performance of hierarchical nanoporous copper and homogeneous nanoporous copper. While the average ligament size and morphology appeared comparable under high-magnification SEM characterization (nanoscale), significant differences were observed at low magnification (micron scale). The lower hydrophobicity of the hierarchical structure enhanced electrolyte interaction, thereby promoting triple-phase reactions and increasing the electrochemical surface area. The bicontinuous nanopores provided superior transport pathways for key intermediates, thereby facilitating C–C coupling and increasing the yield of C_2 products such as ethylene and ethanol. The authors pointed out that mass transport was the dominant factor responsible for the enhanced C_2 product formation. The reaction barrier of the hierarchical structure was lower, enabling the reduction of reaction overpotential. At around -0.704 V (vs RHE), the C_{2+} partial current density of hierarchical structure reached 362 mA/cm^2, compared to 72 mA/cm^2 for homogeneous structure, with Faradaic efficiency of 60% for C_{2+} products[57].

3 Experimental Section

This section covers the experimental design of the whole project, including the sample synthesis, electrode preparation, experimental setup, electrochemical measurements, as well as characterization and product analysis.

3.1 Sample Synthesis

All samples were synthesized by using a simultaneous symmetric thermoanalyzer, a technique capable of monitoring weight loss during the thermal reduction of metal oxides. The process of heat treatment is illustrated in Figure 4. First, 500 mg CuO powder was weighed in a specific crucible (diameter:10 mm) and transferred to a furnace under a reducing atomsphere consisting of 150 mL/min hygroden and 50 mL/min argon. The initial powder was heated at a rate of 10 °C/min to a target temperature, maintained for a specified period, and then cooled to room temperature. Finally, all reduced Cu powder was stored in desiccator to prevent oxidation. By controlling the reduction time and temperature, the CuO powder was fully reduced into Cu powder with different porosity. Notably, the reduction time is the isothermal holding period but not the total heat treatment time. For example, when the powder was heated to the defined temperature and cooled immediately without the isothermal step, the reduction time was recorded as 0 minute. In this project, porous Cu powders were obtained by reducing CuO powder at 250 °C and 300 °C for 0 minute, and 1 hour, respectively.

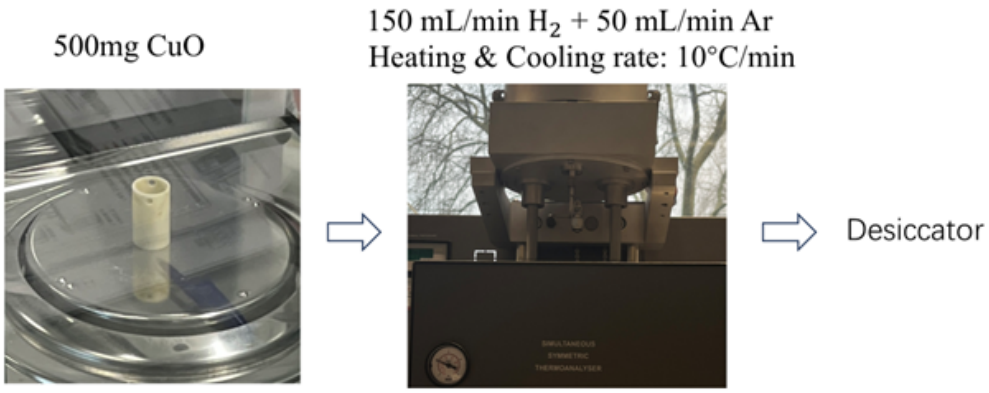

Figure 4: Synthesis process of porous Cu powder.

The reduction degree can be calculated based on the measured weight loss and the theoretical molar mass of the relevant elements. The calculation is expressed as follows:

$$\text{Reduction degree}\,(\%) = \frac{\Delta m_{\text{measured}}}{\Delta m_{\text{theory}}} \times 100\% \tag{4}$$

where

$$\Delta m_{\text{theory}} = m_{\text{initial}} \times \frac{M_{\text{O}}}{M_{\text{CuO}}} \tag{5}$$

Here, $\Delta m_{\text{measured}}$ is the weight loss measured by thermoanalyzer, Δm_{theory} is the theoretical mass loss for 100% reduction of copper oxide, m_{initial} is the initial mass of the sample, M_{O} is the molar mass of oxygen, and M_{CuO} is the molar mass of copper oxide.

3.2 Electrode Preparation

Before starting the electrochemical tests, the powder-electrodes were prepared through the following steps (Figure 5):

(1) Ink preparation. The catalyst ink was prepared by dispersing the sample powders in a mixed solvent with a binder. Specifically, the solvent consisted of a mixture of distilled water and isopropanol in a 1:1 volumetric

ratio. Polytetrafluoroethylene (PTFE, 55 wt%, density = 1.43 g cm^{-3}) was added as a binder at a loading of 10 wt% relative to the powder mass. The suspension was ultrasonicated to ensure homogeneous dispersion.

(2) Drop casting. The prepared ink was deposited onto the substrate by drop casting, which is a widely used technique for fabricating particle-modified electrodes. Carbon paper with a well-defined geometric area of 2.5 cm × 2.5 cm was used as the substrate. The ink was pipetted onto the surface to obtain a uniform catalytic layer, with the loading controlled at 1 mg cm^{-2} for all samples. To accelerate solvent evaporation, the coated substrates were placed on a heating plate maintained at approximately 45°C until completely dried.

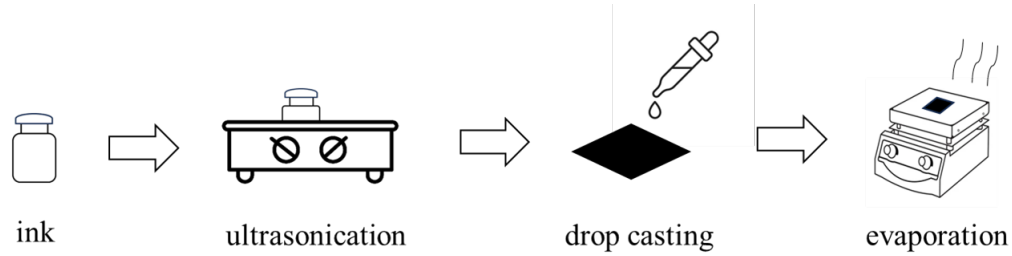

Figure 5: Procedure diagram for electrode preparation.

3.3 Experimental Setup

As an promising technique for electrochemical CO_2 reduction, the gas diffusion electrode (GDE) benefits from the reactions occurring at the three-phase interface, thereby exhibits superior electrocatalytic performance[69]. As displayed in Figure 6, a flow-cell equipped with a three-electrode configuration was employed in this study. The anode consisted of a Pt foil, while the cathode was the prepared powder-based electrode, separated by an anion exchange membrane. And a reference electrode (Ag/AgCl, saturated KCl) was mounted on the flow plate. To enhance the solubility of CO_2 in the electrolyte, the gas flow rate was set as 20 mL min^{-1}. Two peristaltic pumps were used to circulate the anolyte (0.5 M KOH) and catholyte (1 M KOH) at a flow rate of 10 mL min^{-1}. Prior to electrochemical measurements, the electrolyte was saturated with CO_2 for 1.5 h.

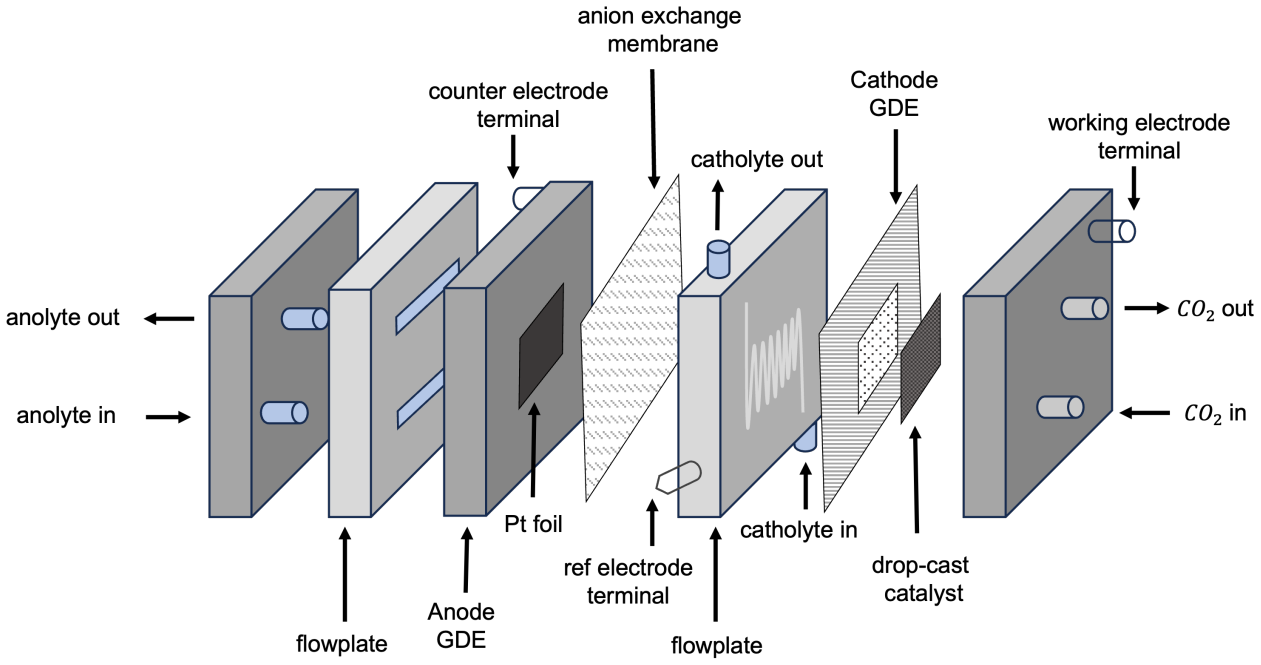

Figure 6: Schematic diagram of experimental setup for GDE.

3.4 Scanning Electron Microscopy (SEM)

As a powerful technique providing qualitative visual images with remarkable resolution, scanning electron microscopy (SEM) is widely employed to investigate the surface phenomena of materials. The superior performance of SEM compared to optical microscopy arises from the much shorter wavelength of the electron beam. When visible light is used as the radiation source, the resolution is inherently limited[70].

In this study, since the materials require higher resolution to reveal nanoscale features, a JEOL JSM-6500F field emission SEM was employed to characterize the pore structure. Sample preparation for SEM is relatively straightforward. Metal powders were uniformly spread as a thin layer on a carbon tape, which was mounted onto a specific sample holder before being transferred into the instrument. Under vacuum conditions, the primary electrons emitted from the electron gun are accelerated into a focused electron beam and directed onto the near-surface region of the sample. The interaction between the incident beam and the sample generates secondary electrons, which are collected by detectors to provide detailed information on the surface morphology[70]. Consequently, high-quality images revealing size, shape, texture, and surface roughness can be obtained, which are critical for the investigation of pore characteristics in this study.

3.5 Brunauer–Emmett–Teller (BET) method

The Brunauer–Emmett–Teller (BET) theory, which is based on the monolayer of close-packed molecules, is commonly applied for surface area determination[71]. The measurement generally involves two steps: (1) pretreatment and (2) analysis.

Pretreatment is carried out to remove moisture and impurities from the sample by degassing. Typically, inert gases such as N_2, Ar, or Kr are used under high-temperature vacuum conditions. A higher degassing temperature (as long as it does not damage the sample structure) generally results in a shorter degassing time[72]. In this study, CuO powder and reduced Cu powders were degassed under N_2 and Kr, respectively, at 120°C for 14 h.

After degassing, the sample cell is transferred to the BET instrument (Micromeritics TriStar II Plus) for measurement. The analysis is conducted at cryogenic conditions, usually using liquid nitrogen as the coolant, which provides stronger interactions with solids compared to other phases and thus ensures a stable low-temperature environment. As illustrated in Figure 7, adsorbates such as N_2 are incrementally introduced into the evacuated sample cell, where adsorption takes place at controlled relative pressures until saturation is reached. Subsequently, the sample is heated to induce desorption of the adsorbed gas[72]. The volume of adsorbed gas is quantified by the data collector to produce a BET isotherm plot, from which the specific surface area was estimated in the relative pressure range between 0.01 and 0.30 in this study.

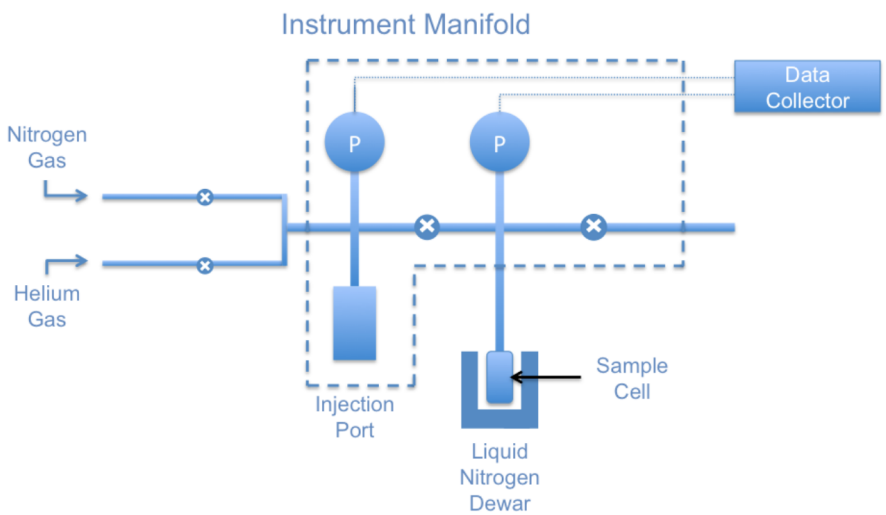

Figure 7: Schematic diagram of BET instrument[72].

3.6 Electrochemical Measurements

3.6.1 Electrochemical Impedance Spectroscopy (EIS)

Electrochemical impedance spectroscopy (EIS) is a practical technique for probing electrochemical systems by converting the real-time response of the system under an applied input signal (current or voltage) into output signals (current or voltage) over a wide range of frequencies. These measurements allow the impedance behavior to be simulated using an equivalent circuit. For instance, in a three-electrode system of this project (Figure 8a), the electrolyte resistance (R_s), the capacitive behavior of the electric double layer (C_{dl}), and the charge-transfer kinetics R_{ct}) at the electrode–electrolyte interface can be represented by passive components of the equivalent circuit model[73].

Typically, the impedance data are presented as Nyquist plots (Figure 8b), which ideally appear as a perfect semicircle. The x-axis corresponds to the real part of the impedance (Z'), and the y-axis corresponds to the imaginary part (Z''). The diameter of the semicircle represents the charge-transfer resistance (R_{ct}), while the intercepts with the real axis at high and low frequencies correspond to the solution resistance (R_s) and the sum $R_s + R_{ct}$, respectively. The maximum of the imaginary component is determined by the combined effects of R_{ct} and the interfacial capacitance (C_{dl})[73, 74].

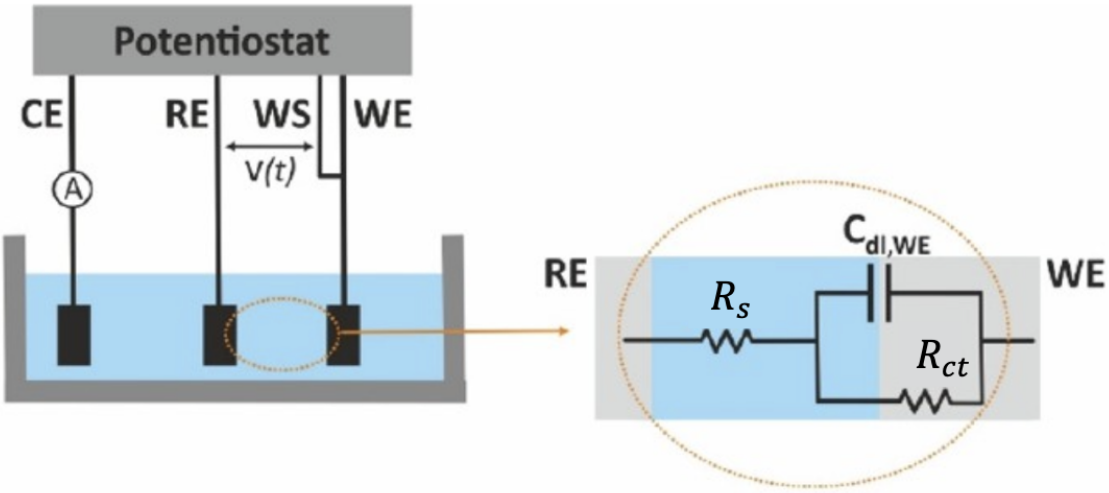

(a) 3-electrodes electrochemical cell and equivalent circuit mode

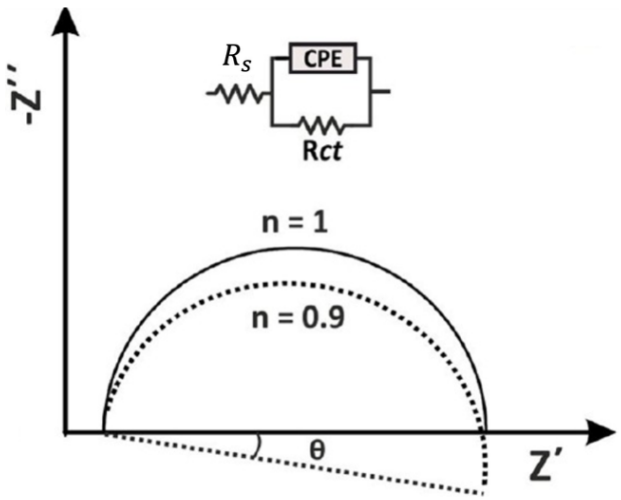

(b) Nyquist plot

Figure 8: Configuration of 3-electrode electrochemical cell and Nyquist plot corresponding to the equivalent circuit.

The roughness and porosity of the electrode can cause a tilt in the impedance spectrum by influencing the solution resistance and interfacial capacitances[73, 75]. In this study, the working electrode has a porous surface; therefore, the ideal capacitor (C_{dl}) is replaced by a constant phase element (CPE) to account for non-ideal capacitive behavior. Potentiostatic Electrochemical Impedance Spectroscopy (PEIS) measurements were performed at the open-circuit potential (OCP) with a probing signal amplitude of 10 mV over a frequency range of 100 kHz to 0.1 Hz, using 30 points per decade. The EIS data were analyzed by EC-lab software.

The double-layer capacitance (C_{CPE}) was extracted from the CPE as the following equation[73]:

$$C_{CPE} = C_f^{1/n} \left(\frac{1}{R_s} + \frac{1}{R_{ct}} \right)^{(n-1)/n} \tag{6}$$

where C_f is the parameter containing the capacitance information (in F s^{n-1}), and n is a constant ranging from 0 to 1, defined by the phase deviation angle θ.

The electrochemical surface area (ECSA) was then calculated as[75]:

$$\text{ECSA} = \frac{C_{CPE}}{C_s} \tag{7}$$

where C_s = 0.4 F m^{-2} is the specific capacitance of 1 M KOH[75, 76, 77].

3.6.2 Linear Sweep Voltammetry (LSV) and Chronoamperometry (CA)

Chronoamperometry with a linear potential sweep, also referred to as linear sweep voltammetry (LSV) or linear scan, is a widely used technique to investigate the electrochemical behavior of materials, particularly for electron-transfer related reactions[78]. In this method, the excitation signal, namely the applied potential and the resulting current at the stationary working electrode, is recorded. The most common representation of the data is a plot of current versus potential. Typically, the potential window is chosen starting from the open-circuit potential (OCP) to ensure a zero-current initial condition. Since current is dependent on electrode size, the measured current is usually normalized by the electrode surface area to allow for comparison. The sign of the current is determined by the scan direction of the applied potential, either positive (anodic sweep) or negative (cathodic sweep)[79]. For small electrodes, the LSV curve often exhibits a plateau-shaped response due to spherical diffusion dominating the electron-transfer process[78].

In this study, LSV measurements were carried out using a VSP-300 potentiostat (Biologic) in a three-electrode system with GDE. The potential was swept from –2.0 V to –0.5 V versus OCP (anodic sweep) at a scan rate of 50 mV s^{-1}.

Chronoamperometry was performed by applying a fixed potential of –1.2 V and –2.5 V versus the reference electrode for 75 min during the catalytic period to monitor the current response and stability of the working electrode.

3.7 Product Analysis

3.7.1 Gas Chromatography (GC)

Gas chromatography (GC) is a widely used technique for both qualitative and quantitative analysis of gaseous products. The resulting chromatogram contains peak heights and areas of adequately resolved signals, from which product identity and distribution can be determined. This allows visualization of the gas product composition and yield in CO_2 reduction experiments[80]. A typical GC instrument consists of three main components: (i) the sample introduction device (injector), (ii) separation columns, and (iii) detectors (Figure 9). After injection, the gaseous products are carried by the carrier gas (Helium or Argon) into the column, where separation occurs based on physicochemical properties such as boiling point, molecular weight/size, polarity, or ionic character. Once separated, each compound produces a characteristic chromatographic peak at a specific retention time. Using the peak area in combination with calibration data, both qualitative and quantitative analysis can be achieved[81].

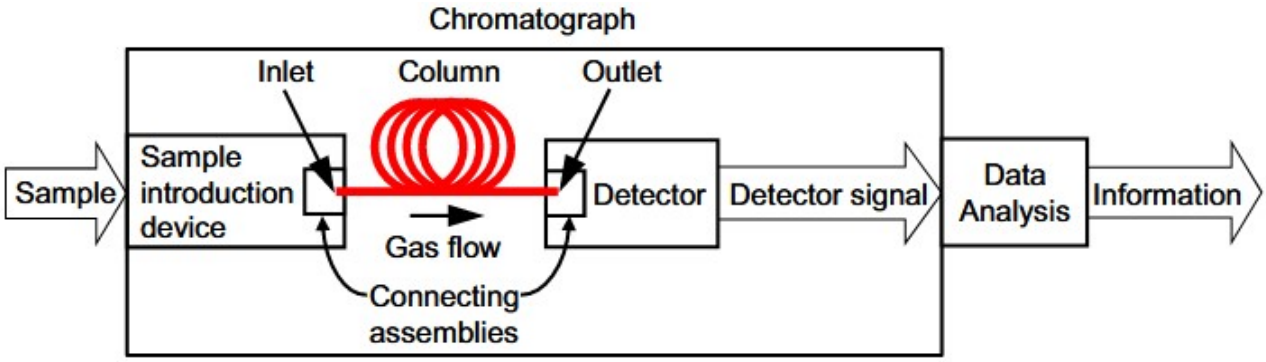

Figure 9: Schematic diagram of a chromatographic system[80]

In this study, a CompactGC 4.0 system was employed, which is equipped with three columns. The first column separates hydrocarbons primarily according to boiling point and vapor pressure and is connected to a flame ionization detector (FID). The other two columns are connected to thermal conductivity detectors (TCD), enabling the identification of gases according to their thermal conductivities. It should be noted that operating parameters such as pressure, temperature, and flow rate can significantly influence the overall analysis process[82]. Therefore, all parameters were carefully maintained at constant values to ensure reproducibility.

This work focuses on the detection of hydrocarbon products from column 1 (FID) and hydrogen from column 3 (TCD), since hydrocarbons are the main targeted CO_2 reduction products of Cu, whereas hydrogen evolution represents the primary competing reaction.

3.7.2 High-Performance Liquid Chromatography (HPLC)

The liquid products were analyzed using High-Performance Liquid Chromatography (HPLC). As illustrated in Figure 10, the general procedure of HPLC is similar to that of GC, except that the samples are in the liquid phase. In HPLC, the carrier gas (mobile phase) used in GC is replaced by an eluent, which is pumped through the system by a high-pressure pump. Between the injector and the analytical column, a guard column is placed to prevent strongly adsorbed sample components from entering the analytical column. Inside the analytical column, the different compounds in the sample are separated based on their retention times, and their concentration variations are subsequently converted into electrical signals by the detector[81].

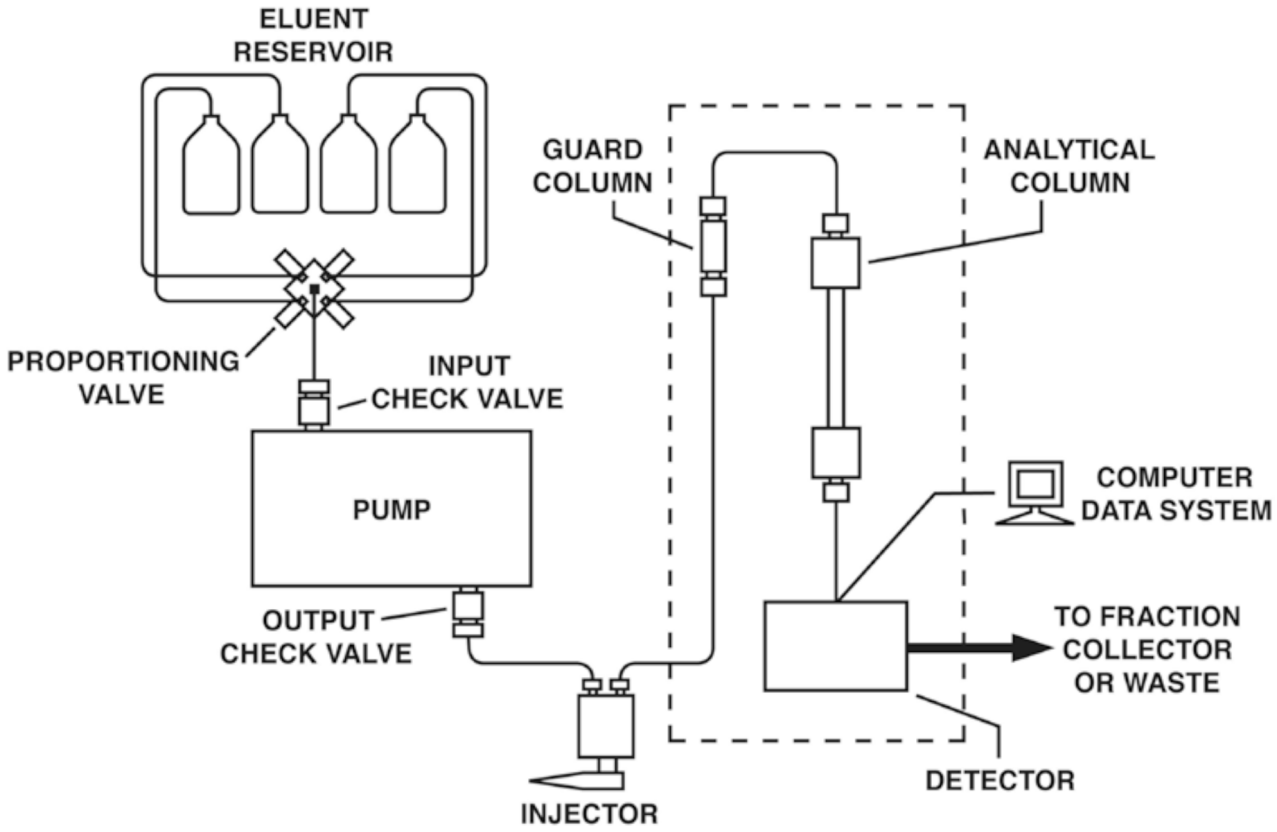

Figure 10: Schematic diagram of a high-performance liquid chromatography[81]

In this study, an Agilent Technologies-1260 Infinity HPLC system was employed for liquid product analysis. The samples, sealed in uniform vials, were stored in an autosampler tray, allowing for automated injection of multiple samples in sequence. A computer-controlled syringe needle withdrew a small aliquot of each liquid sample and introduced it into the column for analysis. Diluted sulfuric acid was used as the eluent, with a flow rate maintained at 0.6 mL min^{-1}. This method was specifically used to identify and quantify liquid CO_2 reduction products, such as formate, ethanol, and other alcohols, complementing the gaseous product analysis performed by GC.

4 Results and Discussion

This section presents and discusses the results of the catalyst synthesis, electrochemical measurements, and product analysis. The experimental methods and analytical principles described in the previous section serve as the foundation for interpreting the structural properties and catalytic performance of the synthesized porous Cu electrodes.

4.1 Reduction Degree

The porous Cu powders were obtained by reducing metal oxides. Since the formation of pores originates from the removal of oxygen from the oxide lattice, and the oxygen content of the precursor oxide is fixed, achieving a complete (100%) reduction is the optimal condition to maximize porosity. To ensure reproducibility under comparable conditions, it is essential to evaluate the reduction degree of the samples.

The calculation method for the reduction degree has been described in the previous section and will not be repeated here. What should be emphasized is that the thermogravimetric analyzer (TGA) measures the total weight loss during the reduction process. In other words, volatile species, such as crystal water or other impurities, may evaporate and interfere with the accuracy of the calculation. To correct for this factor, a control experiment was conducted under identical conditions, except that the reducing atmosphere of 75% H_2 and 25% Ar was replaced by 100% Ar. The weight loss measured in this control run was then subtracted from the total weight loss during reduction, and the corrected reduction degree was calculated, as shown in Figure 11.

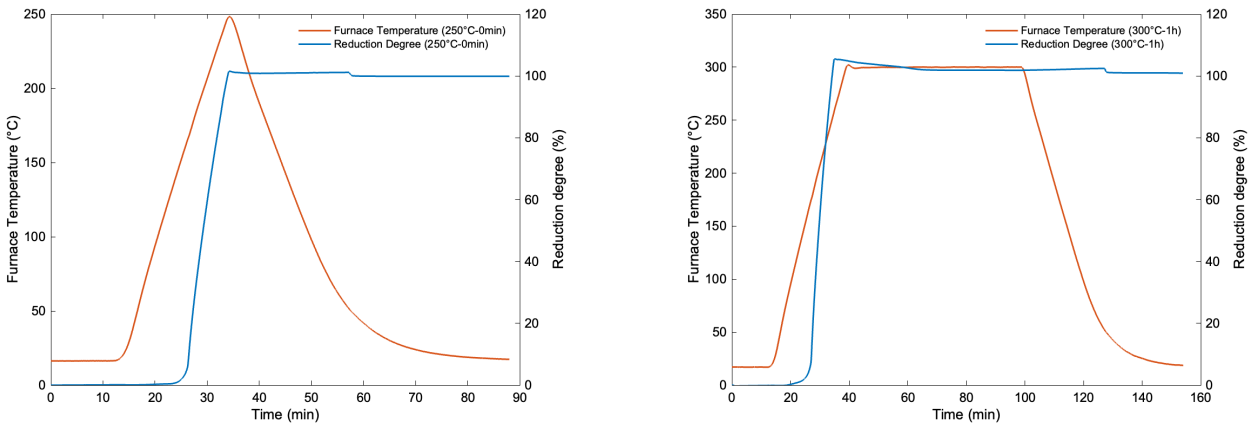

(a) 250 °C-0 min

(b) 300 °C-1 h

Figure 11: Reduction degree and corresponding furnace temperature profiles at different reduction conditions.

It is evident that both treatments resulted in a complete reduction, achieving nearly 100% reduction degree. This confirms that the CuO powder was fully converted into Cu powder. For the sample 250 °C-0 min (Figure 11a), the copper oxide was directly heated to 250 °C and subsequently cooled to room temperature, i.e., without an isothermal step. Similarly, 300 °C-1 h (Figure 11b) corresponds to isothermal holding at 300 °C for 1 h. In both cases, the reduction degree (blue curve) reached 100% at around 250 °C (red curve), when the total reduction time was approximately 35 min. This demonstrates the reliability and reproducibility of the TGA results.

In some instances, the calculated value slightly exceeded 100%, which can be attributed to minor errors in the initial powder mass measurement or instrumental precision. This minor deviation is considered negligible. Additionally, a small decrease in the reduction degree is observed when the furnace temperature approaches room temperature. This effect arises because the reducing atmosphere was terminated during cooling, which may have slightly influenced the TGA measurement.

Moreover, as previously mentioned, the AERO method enables porosity adjustment by controlling the reduction temperature and time. From the TGA results, it is evident that the reduction was completed under the

same conditions. Therefore, the variations in pore structure are likely governed by the interplay between steam diffusion and powder sintering. At elevated temperatures, the stronger expansion and diffusion of vapor gases are expected to generate larger pores. In contrast, with prolonged reduction time, or more precisely, isothermal holding duration, powder sintering becomes dominant, which may lead to pore shrinkage or even disappearance. Consequently, the 250 °C-0 min sample is expected to exhibit smaller but more numerous pores, while the 300 °C-1 h sample is anticipated to contain larger but fewer pores. The characterization of porosity and surface area will be further confirmed in the following section through SEM and BET analyses.

4.2 Surface Morphology and Porosity

The surface morphology, including features such as surface roughness, pore dimensions, and pore distribution, plays a crucial role in determining the catalytic performance of porous copper[64]. In this study, the pore characteristics of the synthesized samples were evaluated using SEM, which provides detailed insights into the porosity at different magnifications, thereby enabling direct comparison between the samples (Figure 12).

At the micrometer scale, the initial CuO powder (Figure 12a) exhibits very small, isolated particles with no visible pores or interparticle connections. In contrast, the reduced foamed Cu powders show rougher surface morphologies. Notably, the 250 °C–0 min sample (Figure 12c) exhibits a continuous, interconnected channel structure, appearing to be the most porous with relatively small pore sizes. The 300 °C–1 h sample (Figure 12e) also displays a porous structure but shows some degree of particle agglomeration, resulting in lower overall porosity but larger pore sizes. At the nanometer scale, the initial CuO powder (Figure 12b) presents tightly packed, needle-like crystals. The pores in the 250 °C–0 min sample (Figure 12d) are very small, less than 100 nm, while those in the 300 °C–1 h sample (Figure 12f) are relatively larger, on the order of several hundred nanometers.

These observation are consistent with the expected behavior of this synthesis method. During thermal reduction of metal oxide, hydrogen diffuses and reacts with oxygen to form steam. At higher temperatures, the expansion is more pronounced, leading to larger pore sizes. Additionally, longer isothermal holding periods promote powder sintering, causing partial pore coalescence and agglomeration, thereby reducing overall porosity.

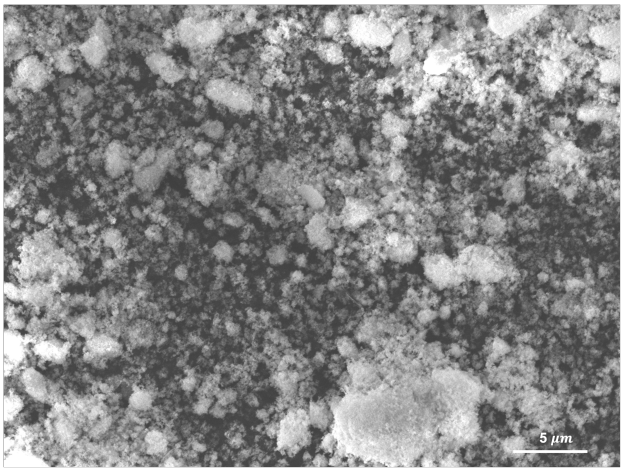

(a) CuO, microscale

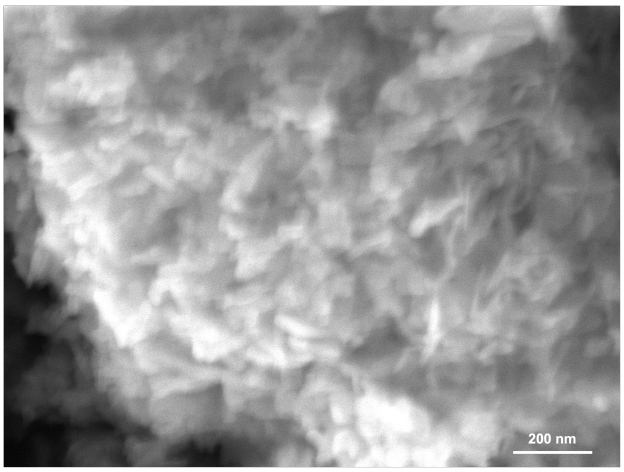

(b) CuO, nanoscale

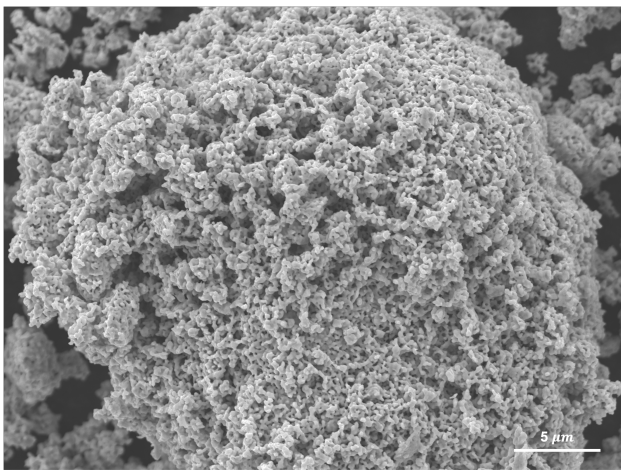

(c) 250 °C–0 min, microscale

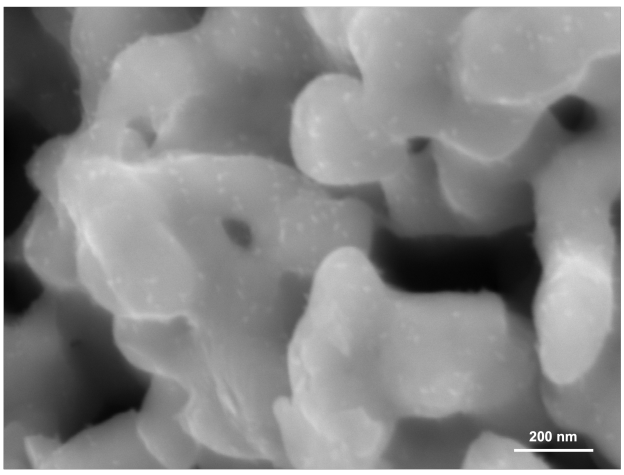

(d) 250 °C–0 min, nanoscale

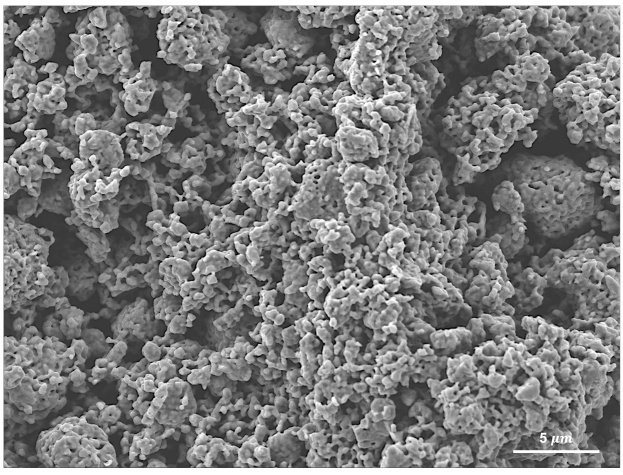

(e) 300 °C–1 h, microscale

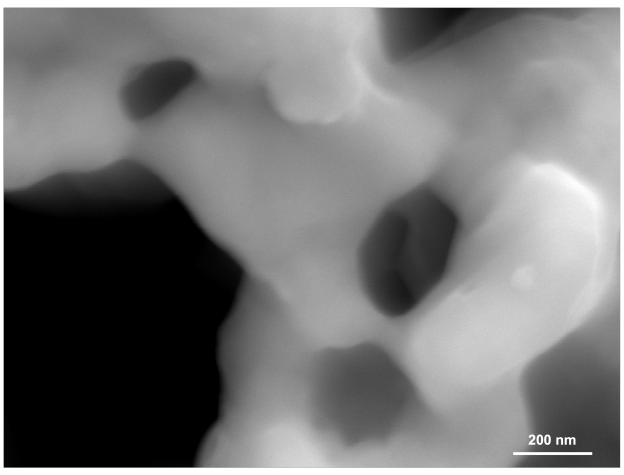

(f) 300 °C–1 h, nanoscale

Figure 12: SEM images of CuO and reduced Cu powders at two magnifications. Microscale images (a, c, e) show overall particle morphology, while nanoscale images (b, d, f) reveal fine crystal features and pore structures.

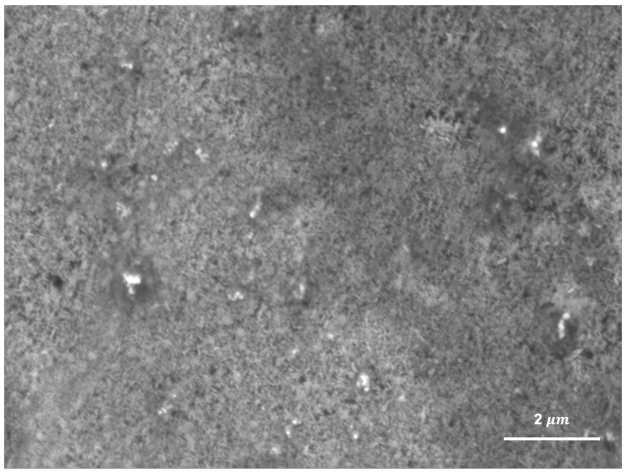

(a) CuO, cross-section

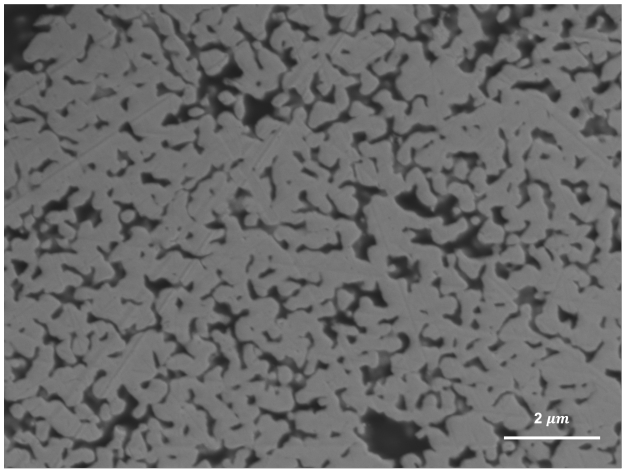

(b) 250 °C–0 min, cross-section

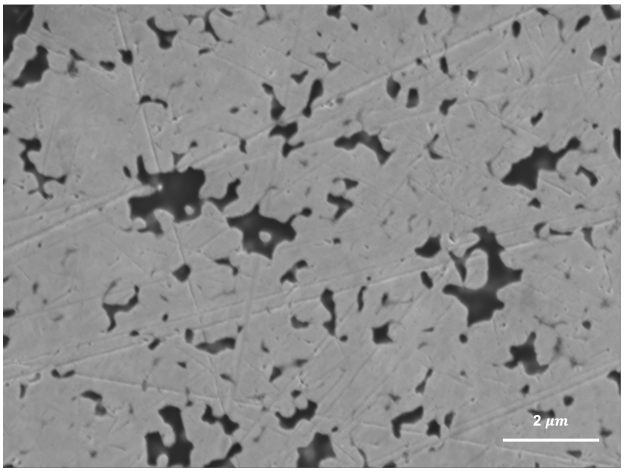

(c) 300 °C–1 h, cross-section

Figure 13: Cross-sectional SEM images of CuO and reduced Cu powders.

To further investigate the internal pore distribution, cross-sectional images of the powder samples were obtained, as shown in Figure 13. The cross-section of the CuO powder reveals a dense and compact morphology. In contrast, the 250 °C–0 min sample exhibits a higher density of interconnected channels with relatively smaller dimensions. The 300 °C–1 h sample also displays a porous cross-section, but with larger and less uniformly distributed channels, which can be attributed to particle agglomeration. These cross-sectional observations are consistent with the porosity evolution discussed in the TGA results and SEM surface morphology images.

To further examine the pore size of the reduced powders, three random regions of each sample were selected during SEM characterization for higher magnification, and the pore sizes were roughly estimated using ImageJ (see Appendix). The average diameter of pores were approximately 78.4 nm for the 250,° C–0 min sample and 273.2 nm for the 300,° C–1 h sample. It should be noted that this estimation is only rough estimates, as the representativeness and statistical reliability of randomly selected sites are limited. In particular, the full range of hierarchical pore sizes cannot be captured by this approach. Therefore, more rigorous methodologies, such as Barrett–Joyner–Halenda (BJH) analysis, will be required in future work to obtain an accurate and reliable pore size distribution. However, for the BJH method, powder agglomeration may significantly affect the results, which will be further discussed in the following section.

Overall, the reduced powders exhibited a porous structure. The 250 °C–0 min sample showed the highest porosity, with an average pore diameter of 78.4 nm. In contrast, the 300 °C–1 h sample displayed a less porous morphology with slight powder agglomeration, accompanied by a larger average pore diameter of 273.2 nm. The SEM characterization results are consistent with the TGA observations, providing mutual confirmation.

4.3 Surface Area

This section investigates the surface area of the samples, including both the intrinsic (physical) surface area of powder and the electrochemically reactive surface area of powder-based electrode.

4.3.1 BET Surface Area

Since the powders in this study are nanoporous, direct measurement of the surface area using SEM or optical microscopy is insufficiently accurate. Therefore, the BET method, which is specifically designed for open internal space measurements, was employed. The BET surface areas of the three sample powders are summarized in Table 2. Nitrogen (N_2) was used as the adsorbate for CuO, while krypton (Kr) was used for the reduced powders. Kr was chosen because its lower saturated vapor pressure allows for more precise measurement of small specific surface areas by the BET method[83].

Table 2: BET results for different catalysts

Sample	Adsorbate	BET SA ($\mathbf{m^2/g}$)
CuO	N_2	24.9905
250 °C-0min	Kr	0.9742
300 °C-1h	Kr	0.6088

Ideally, the reduced porous copper powders are expected to exhibit a larger surface area, as the formation of pores increases the exposed surface. However, in this study, the reduced powders showed a relatively low BET surface area compared to CuO due to the drawbacks of this synthesis method. During high-temperature reduction, the powders tend to agglomerate and form interconnected structures, which significantly increases the particle size and reduces the detectable surface area. This also explains why N_2 was used as the adsorbate to measure CuO[84], as its disproportionate large surface area makes achieving saturation adsorption with Kr difficult, resulting in low measurement efficiency and exceeding the limitations of the BET equipment.

Although the BET surface area of CuO is much larger than that of the reduced powders, a comparison among the reduced samples reveals that the 250 °C–0 min sample exhibits a higher BET surface area than the 300 °C–1 h sample. This observation is consistent with the trends predicted from the TGA and SEM analyses.

4.3.2 Electrochemical Surface Area (ECSA)

While the BET surface area offers valuable information on the physical properties of the samples, its primary value lies in evaluating the effectiveness of the synthesis method. It cannot be directly correlated with the electrochemically active surface area during catalytic reaction. In contrast, electrochemical impedance spectroscopy (EIS) enables the estimation of the electrochemical surface area (ECSA) by determining the capacitance of the electrical double layer. Moreover, EIS data provides insights into the electrical properties and catalytic performance of the powder electrodes.

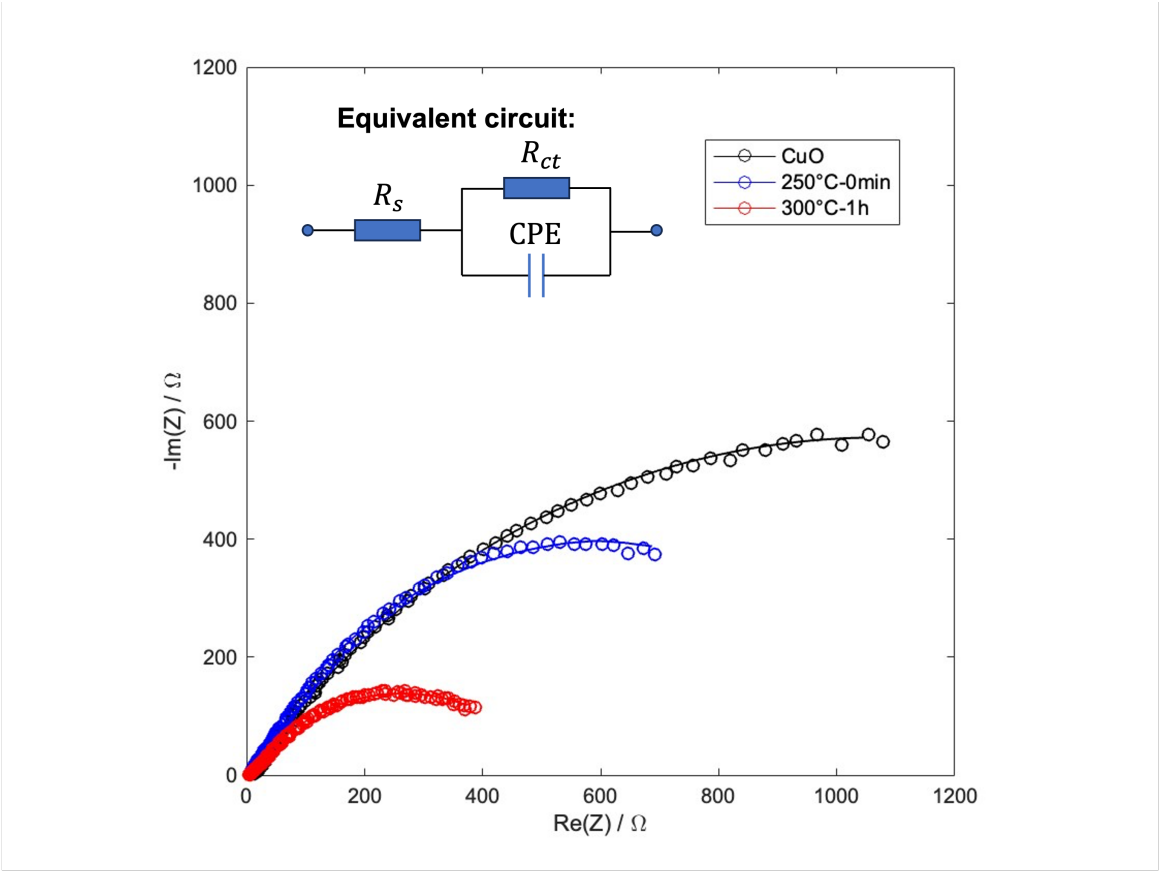

Figure 14: EIS spectra of different samples at open-circuit potential (OCP). Symbols indicate experimental data, while lines represent fitted data.

As explained previously, EIS data is presented by impedance results. In the Nyquist plot (Figure 14), the symbols correspond to the experimental data of the real part of the impedance (Re(Z)) and the imaginary part (Im(Z)), forming a characteristic semicircle. The equivalent circuit model consists of the electrolyte resistance (R_s) in series with the charge-transfer resistance (R_{ct}), which is connected in parallel with the double-layer capacitance (modeled as a constant phase element, CPE). The fitted curves, shown as smooth lines, are obtained by simulating the impedance with equivalent circuit.

Differences in electrode morphology (roughness) and porosity lead to variations in both the ECSA and R_{ct} under identical loading conditions, as summarized in Table 3.

Table 3: EIS results at OCP for different catalysts

Sample	$\boldsymbol{R_{ct}}$ **(Ω)**	$\boldsymbol{C_{dl}}$ (F)	ECSA ($\mathbf{cm^2}$)
CuO	2135	5.4×10^{-4}	13.5
250 °C-0min	1232	6.62×10^{-4}	16.6
300 °C-1h	502	3.20×10^{-4}	8.01

The diameter of the semicircle in the Nyquist plot corresponds to R_{ct}, which reflects the charge-transfer kinetics at the electrode–electrolyte interface. These differences can be attributed to variations in surface morphology and pore size formed during the reduction process. For CuO, the dense thin layer structure hinders charge transfer near electrode, resulting in the largest R_{ct}. In contrast, the restricted smaller pore size of 250 °C–0 min sample limits diffusion, giving rise to an R_{ct} higher than that of the 300 °C–1 h sample but lower than that of CuO.

As summarized in Table 3, the 250 °C–0 min sample exhibits the largest ECSA, whereas the 300 °C–1 h sample

shows the smallest. For 250 °C–0 min sample, it possesses a super porous structure with relatively big amount of pores, which provides the largest ECSA. For the 300 °C–1 h sample, agglomeration during reduction progress leads to a reduced surface area with less pores, which attributes to the smallest ECSA.

In summary, the ECSA results of the porous reduced powder samples are consistent with the BET surface area. However, the non-porous CuO powder shows significant deviations from these measurements. The EIS results further indicate that ECSA and R_{ct} are not directly correlated, as both surface morphology and pore structure play a decisive role in electrochemical behavior.

4.4 Catalytic Activity

The LSV curves record the applied potential and the corresponding current density at the working electrode. The currents were normalized by the ECSA obtained from EIS measurement, ensuring that the catalytic activities of different samples are comparable. As shown in Figure 15, the blue curves correspond to measurements in Ar-saturated electrolyte, whereas the black curves represent measurements in CO_2-saturated electrolyte. In both cases, 1 M KOH was used as the cathodic electrolyte. Under Ar atmosphere, only the hydrogen evolution reaction occurs. In contrast, under CO_2 atmosphere, the CO_2RR competes with HER.

When the blue curve lies above the black curve, i.e., when the current density under Ar is lower than that under CO_2, it indicates that CO_2RR dominates in that applied potential range, implying enhanced catalytic performance. For CuO (Figure 15a), no such potential window is observed, and once the potential reaches approximately −1.2V vs. Ag/AgCl, the current density in Ar rapidly surpasses that in CO_2 as the potential increasing, confirming that HER dominates at more negative potentials. In contrast, for the 250 °C–0 min (Figure 15b) and 300 °C–1 h (Figure 15c) samples, the CO_2RR exceeds HER at around −1.0 V vs. Ag/AgCl. This shift suggests that these oxide-drived Cu catalysts exhibit a lower onset potential or lower overpotential for CO_2RR[85] compared to CuO, thereby favoring CO_2RR over HER.

The superior CO_2RR performance of the reduced samples can be attributed to their porous morphologies. Such structural features increase the number of accessible active sites and facilitate the adsorption and activation of CO_2. Moreover, the presence of structural defects can accelerate charge transfer and stabilize intermediates, which together lower the energetic barrier for CO_2RR[86]. This is reflected in the reduced overpotential of reduced Cu compared with pristine CuO, consistent with the lower R_{ct} values observed in EIS measurements for the porous Cu-based catalysts.

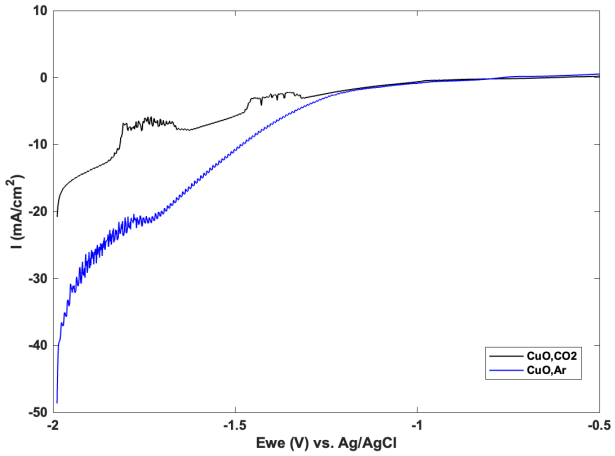

(a) CuO

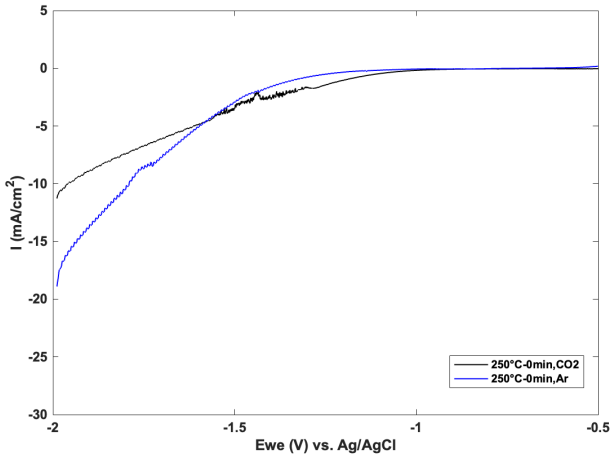

(b) 250 °C–0 min

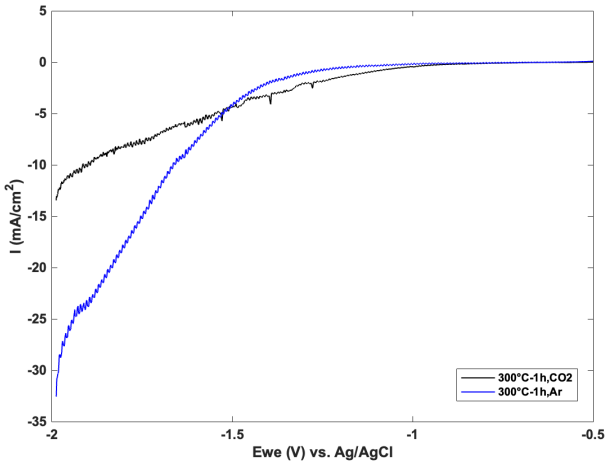

(c) 300 °C–1 h

Figure 15: LSV curves of (a) CuO; (b) 250 °C–0 min; (c) 300 °C–1 h in CO_2/Ar-saturated 1 M KOH.

Comparison of the LSV curves under CO_2 (Figure 16) reveals further insights. At relatively low (less negative) applied potentials, the current densities of the samples are comparable. As the applied potential becomes more negative, CuO exhibits a higher overall current density than the reduced Cu samples. For the CuO sample, two separated peaks are observed on the CO_2RR LSV curve, corresponding to two sequential reduction steps. Specifically, the CuO catalyst is first reduced to Cu^+ species and subsequently to Cu^0 as the potential becomes more negative[87]. This two-step reduction partially induces surface reconstruction of CuO, which is reflected in the variations of the current density.

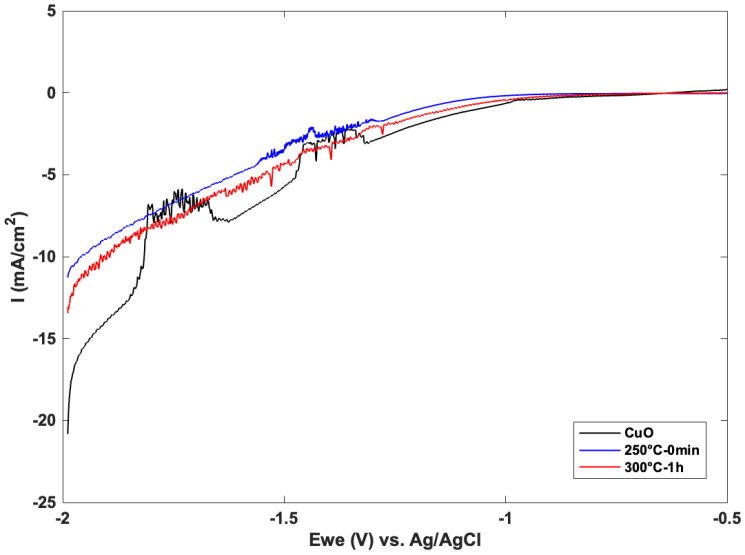

Figure 16: Comparison LSV curves in CO_2

In conclusion, the catalytic activity of the samples follows trends similar to their ECSA values, with the porous catalysts contributing to a reduction in overpotential. It is important to note that the current density measured under CO_2-saturated conditions reflects contributions from both the HER and CO_2RR, and therefore cannot be directly taken as a measure of CO_2RR activity. The LSV curves exhibit noticeable fluctuations, which can be attributed to the predominance of the HER. To further assess catalytic performance, product distribution analysis is required, which will be discussed in the following section.

4.5 Catalytic Stability

Chronoamperometry (CA) was employed to evaluate the catalytic stability. As shown in Figure 17, the measurements were performed at fixed applied potentials of −1.2 V (vs. Ag/AgCl) and −2.5 V (vs. Ag/AgCl) for 75 minutes.

At −1.2 V (Figure 17a), the current densities of the three samples are comparable, consistent with the results obtained from the LSV measurements. In contrast, at −2.5 V (Figure 17b), the 300 °C–1 h sample exhibits the highest current density with pronounced fluctuations. This behavior can be explained by the fact that, at strongly negative potentials, the large driving force activates more reactive sites, and the lowest charge-transfer resistance of the 300 °C–1 h sample facilitates electron transfer. Due to its relatively low porosity with larger pores (273.2 nm), the reaction pathway is dominated by the HER, leading to unstable current responses. Under such conditions, the catalytic kinetics are therefore predominantly governed by HER rather than CO_2RR. In contrast, the 250 °C–0 min sample maintains more stable current densities, suggesting that its porous structure (78.4 nm) effectively stabilizes CO_2RR intermediates and suppresses excessive HER. For CuO samples, the existence of of surface reconstruction may result in an initial increase followed by a decrease in current density. When the reduction is completed, or in other words, when CuO is fully reduced to metallic Cu, the current density tends to stabilize. Nevertheless, all three catalysts demonstrate excellent long-term stability throughout the CA measurement.

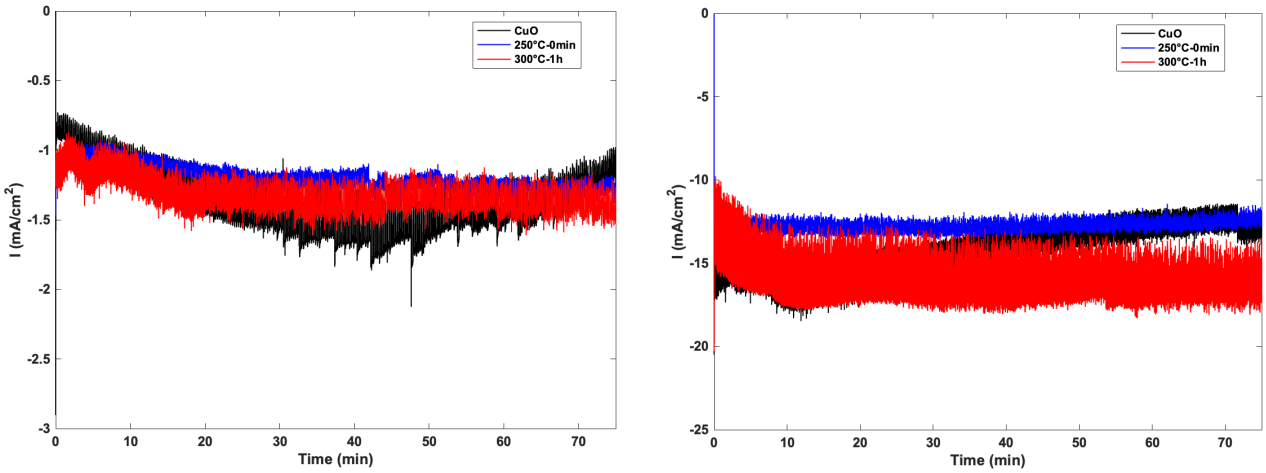

(a) -1.2V (vs Ag/AgCl) (b) -2.5V (vs Ag/AgCl)

Figure 17: CA curves of three samples at (a) -1.2V (vs Ag/AgCl); (b) -2.5V (vs Ag/AgCl).

4.6 Product Analysis

To investigate the selectivity of different samples and elucidate the influence of the nanoporous structure, both gaseous and liquid products of CO_2RR were quantified and compared, as shown in Figure 18.

At an applied potential of -1.2 V, the hydrogen Faradaic efficiency (FE) (Figure 18a) of CuO is higher than that of the porous Cu samples, consistent with the earlier discussion that reduced powder samples lower the energy barrier of CO_2RR at low applied potential. Among all, the 250 °C–0 min catalyst exhibits the lowest HER effect, which may be attributed to its highly porous structure with abundant pore distribution. Such high porosity facilitates the mass transport of alkaline ions, thereby maintaining a locally high pH in the electrolyte microenvironment. This local concentration gradient influences the electrocatalytic process in alkaline media according to the following equilibria[88, 89], which in turn favors CO_2RR over HER. In contrast, the 300 °C–1 h sample, characterized by reduced porosity, shows a weaker ability to suppress HER, though it still exhibits a lower H_2 FE than CuO.

$$CO_2(aq) + OH^- \rightarrow HCO_3^- \tag{8}$$

$$HCO_3^- + OH^- \rightarrow CO_3^{2-} + H_2O \tag{9}$$

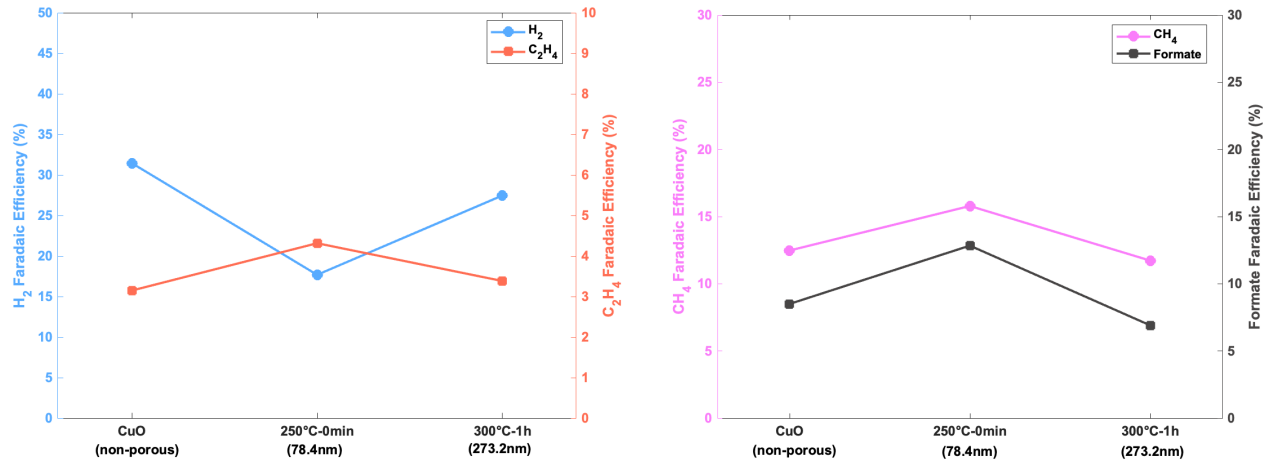

(a) Faradaic effciency of H_2 and C_2H_4 (b) Faradaic effciency of CH_4 and formate

Figure 18: Faradaic effciency of (a) H_2 and C_2H_4; (b) CH_4 and formate at -1.2V (vs Ag/AgCl).

Ethylene (Figure 18a), the only detected C_2 product, demonstrates a strong dependence on the structural characteristics. The 250 °C–0 min sample yields a significantly higher FE for ethylene compared with other samples. This enhancement can be ascribed to the smaller pore size (78.4 nm) than 300 °C–1 h sample (273.2 nm), which prolongs the retention time of key intermediates and reactants, thereby promotes C–C coupling[26]. These results highlight that the nanoconfinement effect plays a decisive role in simultaneously facilitating ethylene formation. Furthermore, they are consistent with the hypothesis that a locally elevated pH can lower the overpotential required for C_2 product generation[89].

The distribution of methane and formate, the only detected liquid product, are shown in Figure 18b. For all three samples, these two C_1 products follow the same trend. The 250 °C–0 min sample displays the highest FEs of both methane and formate, which may be rationalized by its higher porosity that provides more accessible catalytic sites, thereby promotes their production. Meanwhile, the local increased pH leads to the higher proton activity, which acts as the rate-determining step that enhance proton transfer for the C_1 product pathway[89]. Notably, the competition among H_2, CH_4, and formate pathways during CO_2RR results in their inverse selectivity trends.

To better analyze the impact of nanoporosity on product selectivity, the same comparative experiments were conducted at a higher applied potential of –2.5 V vs. Ag/AgCl. The corresponding results are shown in Figure 19.

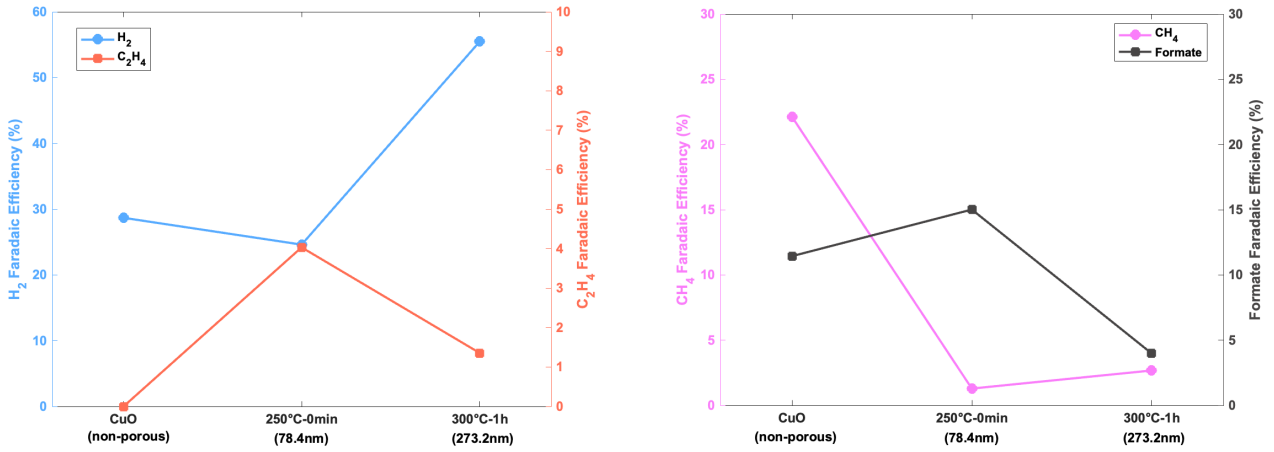

(a) Faradaic effciency of H_2 and C_2H_4

(b) Faradaic effciency of CH_4 and formate

Figure 19: Faradaic effciency of (a) H_2 and C_2H_4; (b) CH_4 and formate at -2.5V (vs Ag/AgCl).

The product distribution at the higher applied potential exhibited significant changes compared to the results at lower potential. Regarding HER (Figure 19a), changes in potential of CuO do not affect mass transport due to the non-porous structure. Consequently, the hydrogen yield remains almost unchanged, in agreement with the observed results. For porous samples, the 250 °C–0 min sample still demonstrated the lowest FE of H_2, in line with expectations. However, the 300 °C–1 h exhibited nearly twice the hydrogen yield of the other samples, this unexpected result that requires further investigation.

For porous structures, high applied potentials lead to a substantial increase in current density, and generate potential differences within the pores which cause local potential gradients. The negatively charged surface result in the accumulation of cations (K^+ in this study), which can impact proton transfer pathways and modify the adsorption energy of key intermediates[89]. The densely packed K^+ ions, being weakly hydrated, reduce hydrogen-bond interactions and consequently inhibit HER[90]. Moreover, the relatively large size of K^+ ions induces a hydrophobic local environment, further promoting CO_2RR over HER[91]. Therefore, for 250 °C–0 min sample, the higher porosity facilitates denser K^+ accumulation, resulting in stronger HER suppression compared to the 300 °C–1 h sample.

Regarding ethylene production (Figure 19a), the 250 °C–0 min sample still exhibits the highest FE, whereas ethylene formation on CuO is almost negligible. This suggests that porous structures retain their advantage in promoting C–C coupling at high potential, whereas the applied potential may be too negative for CuO to

form C_2 products. In addition, the cation effect also plays a significant role for C_2 products, particularly for CO dimerization. The strong local electric field generated by dehydrated K^+ ions stabilizes polarizable intermediates and suppresses their further hydrogenation, thereby favoring C–C coupling pathways[91, 92]. These results further confirm the ecisive influence of nanoconfinement effect on C_2 product formation.

The yields of methane and formate also change under high potential (Figure 19b). Formate production continues to show a negative correlation with HER and same trend with ethylene. The presence of K^+ ions stabilizes the polarized intermediate *COOH, thereby enabling the highly porous 250 °C–0 min sample to achieve the highest FE for formate[91]. For methane, CuO maintains a similar production level, whereas the methane yield on porous copper is significantly reduced. As discussed earlier, during CO_2RR, CuO is reduced to Cu^+ species, which alters the adsorption strength toward H^+ and *CO intermediates[93]. Higher oxidation states of copper favor the formation of the key intermediate *CHO, which subsequently leads to CH_4 production[94]. Moreover, under high OH^- concentration, the Cu^+ species are stabilized and the hydrogenation of *CO is thermodynamically more favorable than dimerization[93]. It has been reported that methane is the dominant product on Cu(I), formed via further hydrogenation of *CO[95]. In contrast, for porous Cu catalysts, the formation of methane is less favorable. Under the cation effect, key intermediates such as *CHO or *COH are less prone to hydrogenation toward CH_4 but confined within the pores, where they interact with each other or with *CO to proceed C–C coupling[96]. This correlated confinement effect is more pronounced for the 250 °C–0 min sample due to its smaller pore size, which facilitates the C-C coupling by prolonging the retention time of key intermediates. These observations collectively indicate that the applied potential exerts a pronounced influence on product distribution, with the effect being dependent on the nanoporosity of the electrode.

In conclusion, nanoporosity affect the product selectivity during CO_2RR. More porous structure can suppress the hydrogen evolution reaction while promoting the formation of C_2 products. At higher applied potential, the influence of nanostructure becomes more pronounced. Regarding competing products with hydrogen, formate selectivity appears slightly affected by nanoporosity and shows an inverse correlation with HER. In contrast, the selectivity toward methane decreases significantly at high applied potentials. The stronger cation effect stablize polarizable species *COOH and lead to weaker connectivity of H-bond network. Moreover, spatial confinement of smaller pores restrict the diffusion and prolong the retention time of key intermediates, favoring C–C coupling. As a result, the 250 °C–0 min sample exhibits lower methane yields but higher formate and ethylene yields compared with the 300 °C–1 h sample. Among CO_2RR products, CO is also an important species. Due to time and technical limitations, this study does not include detection on CO and C_{2+} products, which should be addressed in future work. Including such data would provide a clearer understanding of product distribution and reaction pathway. For example, previous studies have also shown that at low applied potentials, C–C bond formation proceeds via CO dimerization and *CO also plays a significant role on the pathway of CH_4 formation[97, 98]. Moreover, the formation of C_{2+} products warrants attention, copper as a unique catalyst, can produce higher hydrocarbons such as propane and butane under specific conditions[99, 100]. Further discussion on these aspects can be found in the Outlook section of this article.

5 Conclusion

In summary, this study investigated the effect of nanoporosity of Cu powders on CO_2RR selectivity. The project included sample synthesis, electrochemical measurements, and product analysis. Two porous copper powders (250 °C–0 min and 300 °C–1 h) were obtained by controlling reduction time and temperature. Both samples were fully reduced (100%), and SEM analysis revealed average pore sizes of 78.4 nm (250 °C–0 min) and 273.2 nm (300 °C–1 h). However, non-negligible powder agglomeration was also indicated by BET results.

To evaluate catalytic performance, the powders were drop-cast onto GDEs. EIS measurements reflected the charge-transfer resistance and enabled estimation of the ECSA. The high-porosity sample (250 °C–0 min) exhibited the largest ECSA (16.6 cm^2), whereas the low-porosity sample (300 °C–1 h) showed the smallest (8.01 cm^2). The initial CuO displayed an intermediate value of 13.5 cm^2. These results suggest that the ECSA of porous powders was significantly affected by particle agglomeration.

The normalized LSV and CA measurements were employed to probe catalytic activity and stability. The reduced porous powders decreased the onset potential of CO_2RR. Reconstruction of CuO during electrolysis was reflected in the appearance of two peaks in the LSV curve, as well as a gradual decline in current density over time. Nevertheless, all samples maintained reasonable stability for up to 75 minutes.

Product distribution was further analyzed under two applied potentials, –1.2 V and –2.5 V (vs. Ag/AgCl). At the lower potential, no significant differences in selectivity were observed. The most porous sample 250 °C–0 min exhibited the best HER suppression behavior and highest FE of both C_1 and C_2 products due to local pH increase and nanoconfinement effect. At the more negative potential, the 250 °C–0 min sample still exhibited the highest FE for ethylene and the lowest FE for hydrogen. Meanwhile, methane and formate production followed opposite trends relative to HER. Notably, in the high-porosity sample, methane selectivity was significantly reduced, while C_2 products were favored. This can be attributed to both the cation effect and the nanoconfinement effect. The weak H-bond network caused by K^+ accumulation not only lead to suppression of HER and methane, but also contribute to the C-C coupling step. The smaller pore size restricting the diffusion of key intermediates such as *COH and *CHO, thereby prolonging their retention time and promoting C–C coupling.

In short, the porous structure, due to its unique architecture, may cause local electric field and potential gradients, which in turn affect the diffusion and transport of key intermediates or reactants, ultimately influencing reaction pathways and product selectivity. These findings confirm the correlation between nanoporosity and product selectivity. However, a more systematic analysis is still required, and further experiments are necessary to strengthen and generalize these conclusions, as outlined in the following section.

6 Outlook

This chapter discusses the current limitations of the present work and provides suggestions for future research.

6.1 Sample Synthesis

A notable challenge encountered in this study is powder agglomeration, which was clearly reflected in the BET measurements. Ideally, porous copper is expected to exhibit a larger exposed surface area than the initial CuO. To mitigate agglomeration, possible approaches include pre-milling the oxide precursor to further reduce the particle size prior to reduction, or decreasing the batch size of the starting CuO powder. In addition, conducting thermal reduction in larger containers with may help minimize the constraint imposed by the container walls, thereby alleviating particle sintering and aggregation. Beyond these adjustments, advanced fabrication routes such as 3D printing combined with dealloying hold promise for producing hierarchical nanoporous copper powders with more controllable porosity and morphology.

6.2 Experimental Methodology

(1) Drop-casting
In this work, powder-based electrodes were prepared by the drop-casting method. Although convenient and widely used, this method introduces non-negligible uncertainties. Since the study aims to investigate the effect of porosity on CO_2RR, the reproducibility of surface morphology is critical. However, the coffee-ring effect during drying leads to non-uniform particle deposition, potentially reducing the electrochemically active surface area (ECSA) by partial coverage. Such extrinsic porosity may obscure the intrinsic effect of nanoporosity on catalytic performance. Therefore, it is strongly recommended to adopt more advanced techniques, such as air-brush spraying or inkjet printing, which enable more homogeneous and reproducible electrode coatings.

(2) GDE flow cell
The current setup employs screw-based fixation, which is prone to corrosion and uneven force distribution. This occasionally caused gas and electrolyte leakage, leading to undesired energy losses and compromised reproducibility. Future improvements could involve redesigning the sealing components and replacing critical materials to ensure mechanical stability and minimize leakage.

6.3 Future Research Directions

(1) Defects
Porous copper generated by thermal reduction may contain different types and densities of defects (e.g., steps, edges, and vacancies), depending on the reduction conditions. These defects can play an important role in determining catalytic activity and selectivity. Thus, techniques such as XRD and advanced electron microscopy should be employed to further clarify the crystallographic facets and defect distributions.

(2) Reconstruction
During CO_2RR, CuO undergoes in-situ reduction to Cu^+ and Cu^0, which induces surface reconstruction and alters catalytic behavior. Since different oxidation states strongly affect the reaction pathway and product selectivity, using pristine metallic Cu powder as a reference catalyst may provide a more direct and accurate comparison for isolating the effect of porosity.

(3) Potential-dependent selectivity
This study revealed substantial variations in product selectivity at different applied potentials. Future investigations can include systematic measurements across a broader potential range. Coupling experimental results with density functional theory (DFT) calculations would allow for a deeper understanding of adsorption energetics and reaction mechanisms at the active sites.

(4) Pore size quantification
The pore size estimations in this study were based on a limited number of SEM images and lacked strong statistical representation. Future work should adopt more rigorous methodologies, such as Barrett-Joyner-Halenda

(BJH) analysis or advanced 3D tomography techniques, to obtain accurate pore size distributions.

(5) Product analysis
The present product analysis lacked quantification of CO, a crucial intermediate and product in CO_2RR. Including CO detection in future experiments is essential for a more comprehensive analysis. Furthermore, as copper catalysts are capable of producing C_{2+} products, updated calibration files should be employed to achieve more precise quantification of multicarbon products.

Overall, this work highlights the significant role of nanoporosity in governing CO_2RR selectivity. Nevertheless, the summarized challenges cannot be overlooked, and more systematic future research is required. To further investigate the influence of porosity in a more controlled manner, transforming loose powders into mechanically stable pellets could be a promising alternative. In addition, advanced fabrication method such as the combination of 3D printing and dealloying for hierarchical nanoporous powder, may offer an even more effective strategy. In this case, several of the aforementioned external factors would be minimized, allowing for a more rational and accurate evaluation of the intrinsic role of nanoporosity.

References

[1] Daniel J Soeder and Daniel J Soeder. "Fossil fuels and climate change". In: *Fracking and the Environment: A scientific assessment of the environmental risks from hydraulic fracturing and fossil fuels* (2021), pp. 155–185.

[2] Hohyeon Han et al. "Carbon Reduction Method for Intelligent Energy Transformation Based on Energy Data Analysis". In: *2022 IEEE 5th Student Conference on Electric Machines and Systems (SCEMS)*. IEEE. 2022, pp. 1–4.

[3] Chunshan Song. "CO2 conversion and utilization: an overview". In: (2002).

[4] Ahmad Rafiee et al. "Trends in CO2 conversion and utilization: A review from process systems perspective". In: *Journal of environmental chemical engineering* 6.5 (2018), pp. 5771–5794.

[5] A Saravanan et al. "A comprehensive review on different approaches for CO2 utilization and conversion pathways". In: *Chemical Engineering Science* 236 (2021), p. 116515.

[6] Devin T Whipple and Paul JA Kenis. "Prospects of CO2 utilization via direct heterogeneous electrochemical reduction". In: *The Journal of Physical Chemistry Letters* 1.24 (2010), pp. 3451–3458.

[7] Rong-Bin Song et al. "Electrode materials engineering in electrocatalytic CO2 reduction: energy input and conversion efficiency". In: *Advanced Materials* 32.27 (2020), p. 1903796.

[8] Marcel Schreier et al. "Efficient photosynthesis of carbon monoxide from CO2 using perovskite photovoltaics". In: *Nature communications* 6.1 (2015), p. 7326.

[9] Manal F Alqahtani et al. "Porous hollow fiber nickel electrodes for effective supply and reduction of carbon dioxide to methane through microbial electrosynthesis". In: *Advanced Functional Materials* 28.43 (2018), p. 1804860.

[10] Manova Santhosh Yesupatham et al. "Recent Developments in Copper-Based Catalysts for Enhanced Electrochemical CO2 Reduction". In: *Advanced Sustainable Systems* 8.6 (2024), p. 2300549.

[11] Robert Francke and R Daniel Little. "Redox catalysis in organic electrosynthesis: basic principles and recent developments". In: *Chemical Society Reviews* 43.8 (2014), pp. 2492–2521.

[12] Cong Liu, Thomas R Cundari, and Angela K Wilson. "CO2 reduction on transition metal (Fe, Co, Ni, and Cu) surfaces: In comparison with homogeneous catalysis". In: *The Journal of Physical Chemistry C* 116.9 (2012), pp. 5681–5688.

[13] Dong Dong Zhu, Jin Long Liu, and Shi Zhang Qiao. "Recent advances in inorganic heterogeneous electrocatalysts for reduction of carbon dioxide". In: *Advanced materials* 28.18 (2016), pp. 3423–3452.

[14] Sheng Zhang et al. "CO2 reduction: from homogeneous to heterogeneous electrocatalysis". In: *Accounts of chemical research* 53.1 (2020), pp. 255–264.

[15] Gracita M Tomboc et al. "Potential link between Cu surface and selective CO2 electroreduction: perspective on future electrocatalyst designs". In: *Advanced Materials* 32.17 (2020), p. 1908398.

[16] Anthony Vasileff et al. "Surface and interface engineering in copper-based bimetallic materials for selective CO2 electroreduction". In: *Chem* 4.8 (2018), pp. 1809–1831.

[17] Arnau Verdaguer-Casadevall et al. "Probing the active surface sites for CO reduction on oxide-derived copper electrocatalysts". In: *Journal of the American Chemical Society* 137.31 (2015), pp. 9808–9811.

[18] Otmane Zoubir et al. "Current state of copper-based bimetallic materials for electrochemical CO 2 reduction: a review". In: *RSC advances* 12.46 (2022), pp. 30056–30075.

[19] Ruo-Zheng Xiong et al. "Recent progress in Cu-based electrocatalysts for CO2 reduction". In: *Chemical Engineering Journal* (2025), p. 159210.

[20] Eden EL Tanner and Richard G Compton. "How can electrode surface modification benefit electroanalysis?" In: *Electroanalysis* 30.7 (2018), pp. 1336–1341.

[21] Zhengxiang Gu et al. "Efficient electrocatalytic CO2 reduction to C2+ alcohols at defect-site-rich Cu surface". In: *Joule* 5.2 (2021), pp. 429–440.

[22] Jiawei Liu et al. "Directing the architecture of surface-clean Cu2O for CO electroreduction". In: *Journal of the American Chemical Society* 144.27 (2022), pp. 12410–12420.

[23] Shangqian Zhu et al. "Recent advances in catalyst structure and composition engineering strategies for regulating CO2 electrochemical reduction". In: *Advanced Materials* 33.50 (2021), p. 2005484.

[24] Jinxi Chen et al. “Composition-tuned surface binding on CuZn-Ni catalysts boosts CO2RR selectivity toward CO generation”. In: *ACS Materials Letters* 4.3 (2022), pp. 497–504.

[25] Wenli Su, Weizan Guo, and Yu Fan. “CuAg bimetallic catalysts derived from an Ag-anchored Cu-based metal–organic framework for CO2 electroreduction to ethanol”. In: *Chemical Engineering Journal* 477 (2023), p. 147204.

[26] Wesley Luc and Feng Jiao. “Nanoporous metals as electrocatalysts: state-of-the-art, opportunities, and challenges”. In: *ACS Catalysis* 7.9 (2017), pp. 5856–5861.

[27] Hui Chen et al. “Active site engineering in porous electrocatalysts”. In: *Advanced Materials* 32.44 (2020), p. 2002435.

[28] Mark A Atwater, Kris A Darling, and Mark A Tschopp. “Solid-State Foaming by Oxide Reduction and Expansion: Tailoring the Foamed Metal Microstructure in the Cu–CuO System with Oxide Content and Annealing Conditions”. In: *Advanced Engineering Materials* 18.1 (2016), pp. 83–95.

[29] Mark A Atwater et al. “Solid state porous metal production: a review of the capabilities, characteristics, and challenges”. In: *Advanced Engineering Materials* 20.7 (2018), p. 1700766.

[30] Jiawei Dai et al. “Structural Regulating of Cu-Based Metallic Electrocatalysts for CO2 to C2+ Products Conversion”. In: *ChemSusChem* 18.9 (2025), e202402184.

[31] Xiaolong Zhang et al. “Electrocatalytic carbon dioxide reduction: from fundamental principles to catalyst design”. In: *Materials Today Advances* 7 (2020), p. 100074.

[32] Abebe Reda Woldu et al. “Electrochemical CO2 reduction (CO2RR) to multi-carbon products over copper-based catalysts”. In: *Coordination Chemistry Reviews* 454 (2022), p. 214340.

[33] Kendra P Kuhl et al. “New insights into the electrochemical reduction of carbon dioxide on metallic copper surfaces”. In: *Energy & Environmental Science* 5.5 (2012), pp. 7050–7059.

[34] Wei Xia et al. “Adjacent copper single atoms promote C–C coupling in electrochemical CO2 reduction for the efficient conversion of ethanol”. In: *Journal of the American Chemical Society* 145.31 (2023), pp. 17253–17264.

[35] Yu-Jhih Shen et al. “Microenvironment Matters: Copper–Carbon Composites Enable a Highly Efficient Carbon Dioxide Reduction Reaction to C2 Products”. In: *ACS Applied Materials & Interfaces* (2025).

[36] Yanan Cao et al. “Stimulating the C- C coupling ability of ultrafine copper nanoclusters via nitrogen coordination for electrocatalytic CO2 reduction”. In: *Applied Catalysis B: Environment and Energy* 361 (2025), p. 124704.

[37] Douglas R Kauffman et al. “Selective electrocatalytic reduction of CO2 into CO at small, thiol-capped Au/Cu nanoparticles”. In: *The Journal of Physical Chemistry C* 122.49 (2018), pp. 27991–28000.

[38] Sibo Shen et al. “AuCu alloy nanoparticle embedded Cu submicrocone arrays for selective conversion of CO2 to ethanol”. In: *Small* 15.37 (2019), p. 1902229.

[39] Zhiyuan Chang et al. “The tunable and highly selective reduction products on Ag@ Cu bimetallic catalysts toward CO2 electrochemical reduction reaction”. In: *The Journal of Physical Chemistry C* 121.21 (2017), pp. 11368–11379.

[40] Yanzhi Xu et al. “Tuning the selectivity of liquid products of CO2RR by Cu–Ag alloying”. In: *ACS Applied Materials & Interfaces* 14.9 (2022), pp. 11567–11574.

[41] Yurui Xu et al. “Achieving high selectivity and activity of CO2 electroreduction to formate by in-situ synthesis of single atom Pb doped Cu catalysts”. In: *Journal of Colloid and Interface Science* 665 (2024), pp. 365–375.

[42] Dan Ren, Bridget Su-Hui Ang, and Boon Siang Yeo. “Tuning the selectivity of carbon dioxide electroreduction toward ethanol on oxide-derived Cu x Zn catalysts”. In: *Acs Catalysis* 6.12 (2016), pp. 8239–8247.

[43] Hyo Sang Jeon et al. “Operando insight into the correlation between the structure and composition of CuZn nanoparticles and their selectivity for the electrochemical CO2 reduction”. In: *Journal of the American Chemical Society* 141.50 (2019), pp. 19879–19887.

[44] Hakhyeon Song et al. “Tunable product selectivity in electrochemical CO2 reduction on well-mixed Ni–Cu alloys”. In: *ACS Applied Materials & Interfaces* 13.46 (2021), pp. 55272–55280.

[45] Qi Lu et al. “Highly porous non-precious bimetallic electrocatalysts for efficient hydrogen evolution”. In: *Nature communications* 6.1 (2015), p. 6567.

[46] Maolin Zhang et al. “Tunable selectivity for electrochemical CO2 reduction by bimetallic Cu–Sn catalysts: elucidating the roles of Cu and Sn”. In: *ACS Catalysis* 11.17 (2021), pp. 11103–11108.

[47] Qiuyu Zhao et al. “In situ reconstruction of Bi nanoparticles confined within 3D nanoporous Cu to boost CO2 electroreduction”. In: *Science China Materials* 67.3 (2024), pp. 796–803.

[48] Wenjin Zhu et al. “Morphological and compositional design of Pd–Cu bimetallic nanocatalysts with controllable product selectivity toward CO2 electroreduction”. In: *Small* 14.7 (2018), p. 1703314.

[49] Taozhi Sun et al. “Selectivities of stepped Cu–M (M= Pt, Ni, Pd, Zn, Ag, Au) bimetallic surface environment for C1 and C2 pathways”. In: *Langmuir* 40.17 (2024), pp. 9289–9298.

[50] Erlend Bertheussen et al. “Electroreduction of CO on polycrystalline copper at low overpotentials”. In: *ACS Energy Letters* 3.3 (2018), pp. 634–640.

[51] Shanwen Wang et al. “Recent progress in electrochemical reduction of CO2 by oxide-derived copper catalysts”. In: *Materials Today Nano* 12 (2020), p. 100096.

[52] Christina W Li and Matthew W Kanan. “CO2 reduction at low overpotential on Cu electrodes resulting from the reduction of thick Cu2O films”. In: *Journal of the American Chemical Society* 134.17 (2012), pp. 7231–7234.

[53] Daixing Wei et al. “Surface Adsorbed Hydroxyl: A Double-Edged Sword in Electrochemical CO2 Reduction Over Oxide-Derived Copper”. In: *Angewandte Chemie International Edition* 62.31 (2023), e202306876.

[54] Chunmiao Ye et al. “Enhanced electrochemical CO2 reduction to formate on poly (4-vinylpyridine)-modified copper and gold electrodes”. In: *ACS applied materials & interfaces* 14.40 (2022), pp. 45263–45271.

[55] Tete Zhao et al. “Functionalizing Cu nanoparticles with fluoric polymer to enhance C2+ product selectivity in membraned CO2 reduction”. In: *Applied Catalysis B: Environmental* 340 (2024), p. 123281.

[56] Jinmeng Li et al. “Polyquinone modification promotes CO2 activation and conversion to C2+ products over copper electrode”. In: *ACS Energy Letters* 7.11 (2022), pp. 4045–4051.

[57] Wen-Han Tsai et al. “Evaluating diffusivity for efficient electrocatalytic conversion of carbon dioxide into multicarbon products using dealloyed hierarchically nanoporous copper”. In: *Applied Surface Science* 679 (2025), p. 161215.

[58] Yan Kong et al. “Diffusion Retardation Induced by Steric Confinement to Accelerate CO2 Electroreduction Towards Multicarbon Products”. In: *CCS Chemistry* 7.4 (2025), pp. 1227–1239.

[59] Peng-Peng Yang et al. “Protecting copper oxidation state via intermediate confinement for selective CO2 electroreduction to C2+ fuels”. In: *Journal of the American Chemical Society* 142.13 (2020), pp. 6400–6408.

[60] Yongzhi Zhong et al. “Adjusting local CO confinement in porous-shell Ag@ Cu catalysts for enhancing C–C coupling toward CO2 eletroreduction”. In: *Nano Letters* 22.6 (2022), pp. 2554–2560.

[61] Fuping Pan et al. “Long-Range Confinement-Driven Enrichment of Surface Oxygen-Relevant Species Promotes C- C Electrocoupling in CO2 Reduction”. In: *Advanced Energy Materials* 14.7 (2024), p. 2303118.

[62] Wei Tang et al. “The importance of surface morphology in controlling the selectivity of polycrystalline copper for CO2 electroreduction”. In: *Physical Chemistry Chemical Physics* 14.1 (2012), pp. 76–81.

[63] Abhijit Dutta et al. “Morphology matters: tuning the product distribution of CO2 electroreduction on oxide-derived Cu foam catalysts”. In: *AcS catalysis* 6.6 (2016), pp. 3804–3814.

[64] Jidsucha Darayen et al. “Porous electrodeposited Cu as a potential electrode for electrochemical reduction reactions of CO2”. In: *Applied Sciences* 11.23 (2021), p. 11104.

[65] Yuecheng Peng et al. “Selective electrochemical reduction of CO2 to ethylene on nanopores-modified copper electrodes in aqueous solution”. In: *ACS applied materials & interfaces* 9.38 (2017), pp. 32782–32789.

[66] Sujat Sen, Dan Liu, and G Tayhas R Palmore. “Electrochemical reduction of CO2 at copper nanofoams”. In: *Acs Catalysis* 4.9 (2014), pp. 3091–3095.

[67] Ki Dong Yang et al. “Morphology-directed selective production of ethylene or ethane from CO2 on a Cu mesopore electrode”. In: *Angewandte Chemie* 129.3 (2017), pp. 814–818.

[68] Yao Tan et al. “Near-Electrode Concentration Gradients of Bicarbonate and pH within Porous Gas Diffusion Electrode for Optimized Selective CO2 Electroreduction to C2+ Products”. In: *Nano Letters* 24.39 (2024), pp. 12163–12170.

[69] Hesamoddin Rabiee et al. “Advances and challenges of carbon-free gas-diffusion electrodes (GDEs) for electrochemical CO2 reduction”. In: *Advanced Functional Materials* 35.1 (2025), p. 2411195.

[70] Kalsoom Akhtar et al. “Scanning electron microscopy: Principle and applications in nanomaterials characterization”. In: *Handbook of materials characterization*. Springer, 2018, pp. 113–145.

[71] D Dollimore, P Spooner, and AJST Turner. “The bet method of analysis of gas adsorption data and its relevance to the calculation of surface areas”. In: *Surface Technology* 4.2 (1976), pp. 121–160.

[72] Nina Hwang and Andrew R Barron. “BET surface area analysis of nanoparticles”. In: *The connexions project* 1 (2011).

[73] Alexandros Ch Lazanas and Mamas I Prodromidis. “Electrochemical impedance spectroscopy— a tutorial”. In: *ACS measurement science au* 3.3 (2023), pp. 162–193.

[74] Samuel Cruz-Manzo and Rui Chen. “A generic electrical circuit for performance analysis of the fuel cell cathode catalyst layer through electrochemical impedance spectroscopy”. In: *Journal of Electroanalytical Chemistry* 694 (2013), pp. 45–55.

[75] Guangfu Li et al. “New insights into evaluating catalyst activity and stability for oxygen evolution reactions in alkaline media”. In: *Sustainable Energy & Fuels* 2.1 (2018), pp. 237–251.

[76] Atanu Roy et al. “Influence of electrochemical active surface area on the oxygen evolution reaction and energy storage performance of MnO2-multiwalled carbon nanotube composite”. In: *International Journal of Energy Research* 45.11 (2021), pp. 16908–16921.

[77] Poulami Mukherjee et al. “Anchoring MoS 2 on an ethanol-etched Prussian blue analog for enhanced electrocatalytic efficiency for the oxygen evolution reaction”. In: *Materials Chemistry Frontiers* 6.13 (2022), pp. 1770–1778.

[78] Bernd Speiser. “Linear Sweep and Cyclic Voltammetry”. In: *Encyclopedia of Electrochemistry: Online* (2007).

[79] G Bontempelli, N Dossi, and R Toniolo. “Linear sweep and cyclic”. In: (2016).

[80] Leonid M Blumberg. “Theory of gas chromatography”. In: *Gas chromatography*. Elsevier, 2021, pp. 19–97.

[81] Bradley L Reuhs. “High-performance liquid chromatography”. In: *Food analysis*. Springer, 2017, pp. 213–226.

[82] Colin F Poole. “Column classification and structure-retention relationships”. In: *Gas Chromatography*. Elsevier, 2021, pp. 165–190.

[83] Hiroshi Yanazawa, Katsushi Ohshika, and Toshiharu Matsuzawa. “Precision evaluation in kr adsorption for small bet surface area measurements of less than 1 m2”. In: *Adsorption* 6.1 (2000), pp. 73–77.

[84] Wan Nor Roslam Wan Isahak et al. “Adsorption–desorption of CO2 on different type of copper oxides surfaces: Physical and chemical attractions studies”. In: *Journal of CO2 Utilization* 2 (2013), pp. 8–15.

[85] Oriol Piqué et al. “Computational-experimental study of the onset potentials for CO2 reduction on polycrystalline and oxide-derived copper electrodes”. In: *Electrochimica Acta* 380 (2021), p. 138247.

[86] Khanh-Ly C Nguyen et al. “The Influence of Mesoscopic Surface Structure on the Electrocatalytic Selectivity of CO2 Reduction with UHV-Prepared Cu (111) Single Crystals”. In: *ACS Energy Letters* 9.2 (2024), pp. 644–652.

[87] Haojun Shi et al. “Stabilizing Cu+ species in Cu2O/CuO catalyst via carbon intermediate confinement for selective CO2RR”. In: *Advanced Functional Materials* 34.11 (2024), p. 2310913.

[88] Akansha Goyal et al. “Effect of pore diameter and length on electrochemical CO 2 reduction reaction at nanoporous gold catalysts”. In: *Chemical Science* 13.11 (2022), pp. 3288–3298.

[89] Stephanie Nitopi et al. “Progress and perspectives of electrochemical CO2 reduction on copper in aqueous electrolyte”. In: *Chemical reviews* 119.12 (2019), pp. 7610–7672.

[90] Xueping Qin, Tejs Vegge, and Heine Anton Hansen. “Cation-coordinated inner-sphere CO2 electroreduction at Au–water interfaces”. In: *Journal of the American Chemical Society* 145.3 (2023), pp. 1897–1905.

[91] Qian Wu and Zhichuan J Xu. “Mechanistic Insights into Cation Effects in Electrolytes for Electrocatalysis”. In: *Angewandte Chemie International Edition* (2025), e202505022.

[92] Gumaa A El-Nagar et al. “Unintended cation crossover influences CO2 reduction selectivity in Cu-based zero-gap electrolysers”. In: *Nature communications* 14.1 (2023), p. 2062.

[93] Jong-Yeong Jung et al. "Switching Methane Selectivity in Carbon Dioxide Electroreduction via Confining Copper (I) Oxide Nanocubes by Polyimine Shells". In: *ACS Catalysis* 15.3 (2025), pp. 2642–2653.

[94] Fan Yang et al. "Optimizing copper oxidation state to promote ethylene generation in efficient carbon dioxide conversion". In: *ACS Sustainable Chemistry & Engineering* 10.14 (2022), pp. 4677–4682.

[95] Tsu-Chin Chou et al. "Controlling the oxidation state of the Cu electrode and reaction intermediates for electrochemical CO2 reduction to ethylene". In: *Journal of the American Chemical Society* 142.6 (2020), pp. 2857–2867.

[96] Xiaowen Min et al. "Porous metal nanocrystal catalysts: can crystalline porosity enable catalytic selectivity?" In: *CCS Chemistry* 4.6 (2022), pp. 1829–1842.

[97] Jason D Goodpaster, Alexis T Bell, and Martin Head-Gordon. "Identification of possible pathways for C–C bond formation during electrochemical reduction of CO2: new theoretical insights from an improved electrochemical model". In: *The journal of physical chemistry letters* 7.8 (2016), pp. 1471–1477.

[98] Xiaowa Nie et al. "Selectivity of CO 2 Reduction on Copper Electrodes: The Role of the Kinetics of Elementary Steps." In: *Angewandte Chemie International Edition* 52.9 (2013).

[99] Tao-Tao Zhuang et al. "Copper nanocavities confine intermediates for efficient electrosynthesis of C3 alcohol fuels from carbon monoxide". In: *Nature Catalysis* 1.12 (2018), pp. 946–951.

[100] Simon D Rihm et al. "On the role of C 4 and C 5 products in electrochemical CO 2 reduction via copper-based catalysts". In: *Energy & Environmental Science* 16.4 (2023), pp. 1697–1710.

Appendix

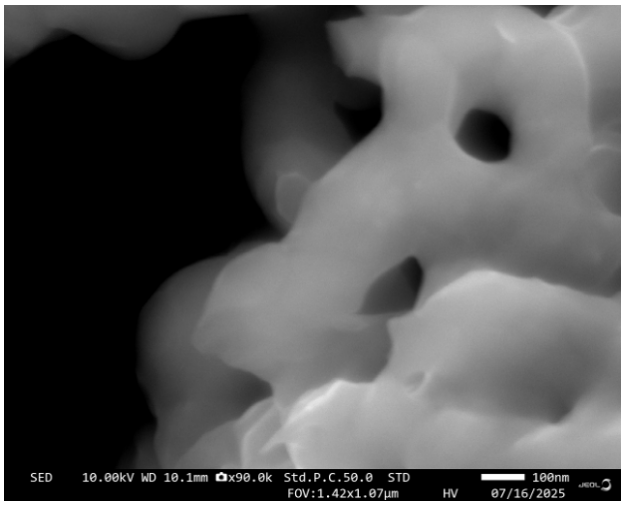

(a) 250 °C-0min, 90k

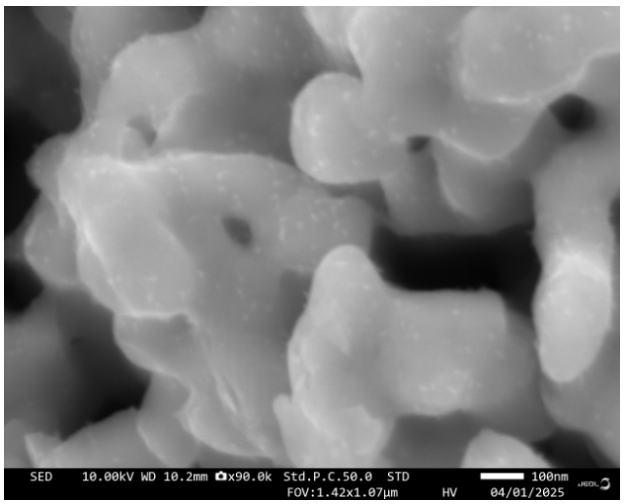

(b) 250 °C-0min, 90k

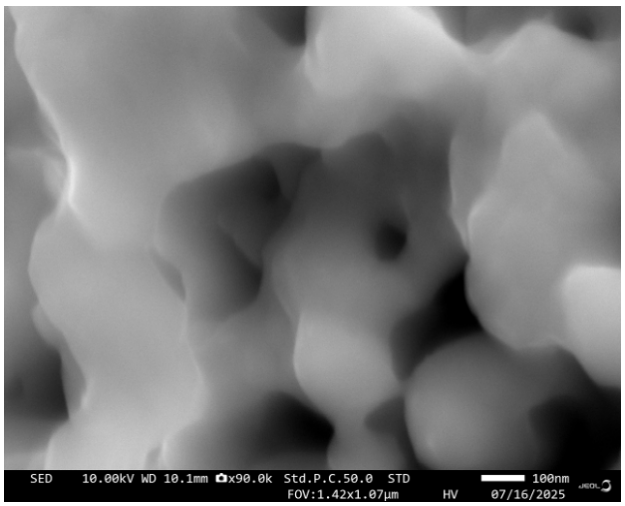

(c) 250 °C-0min, 90k

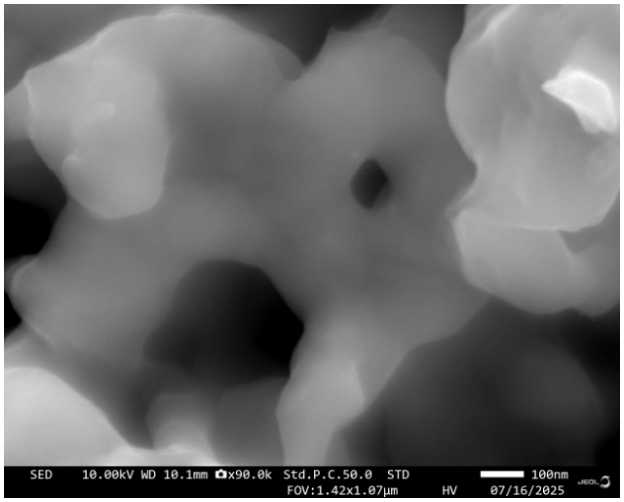

(d) 250 °C-0min, 90k

Figure 20: SEM images of 250 °C-0min at same magnification.

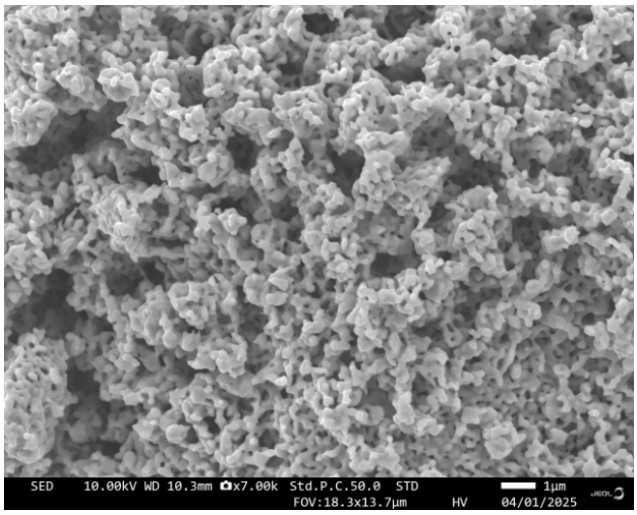

(a) 250 °C-0min, 7k

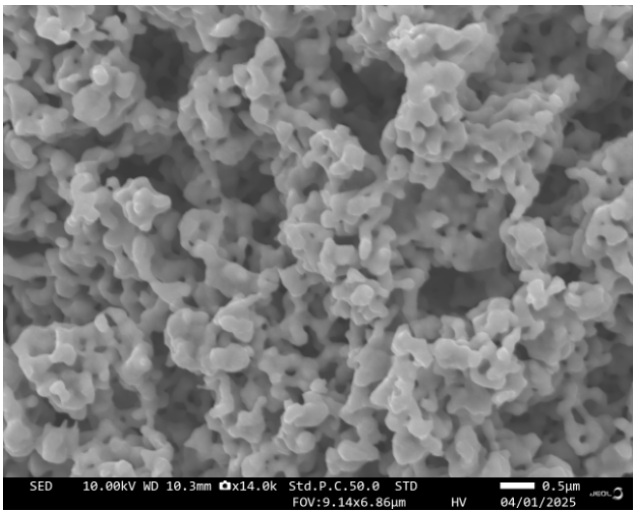

(b) 250 °C–0 min, 14k

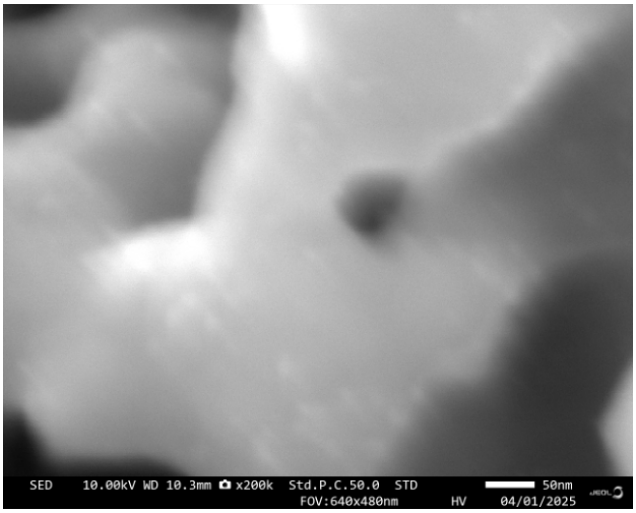

(c) 250 °C–0 min, 200k

Figure 21: SEM images of 250 °C-0min at different magnifications.

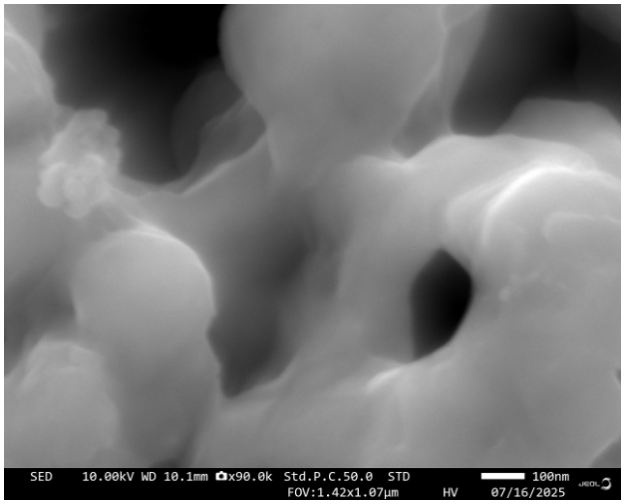

(a) 300 °C–1 h, 90k

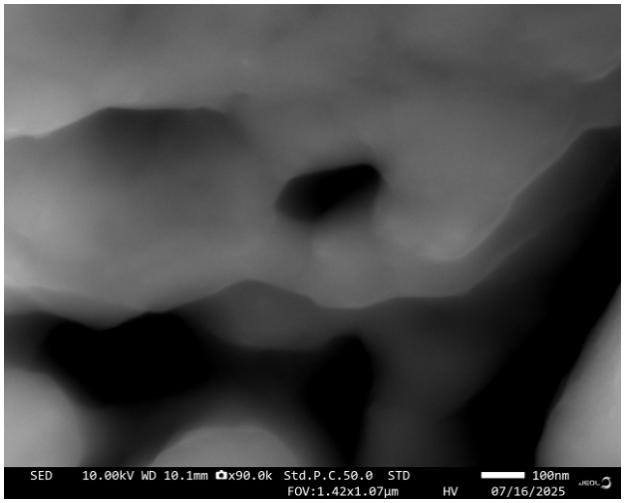

(b) 300 °C–1 h, 90k

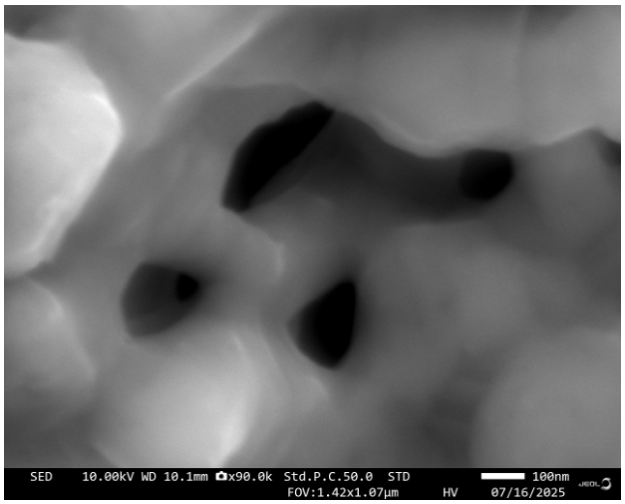

(c) 300 °C–1 h, 90k

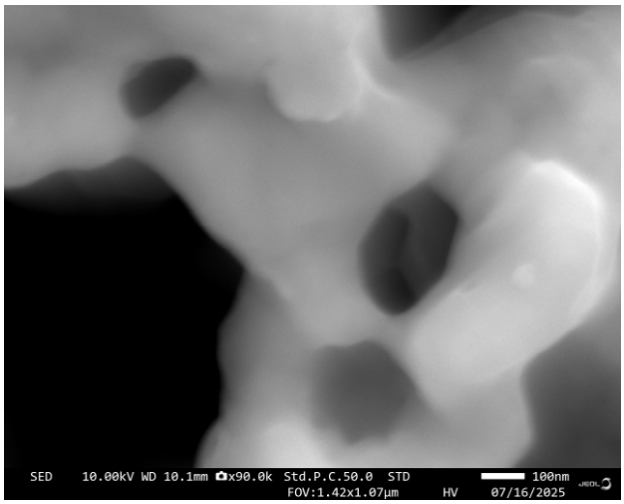

(d) 300 °C–1 h, 90k

Figure 22: SEM images of 300 °C–1 h at same magnification.

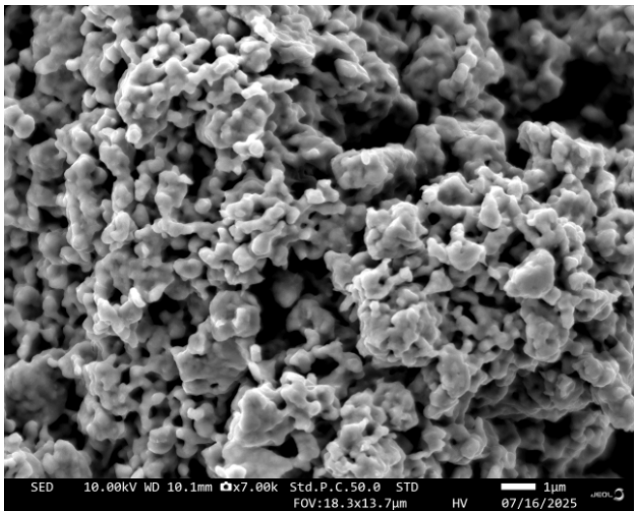

(a) 300 °C–1 h, 7k

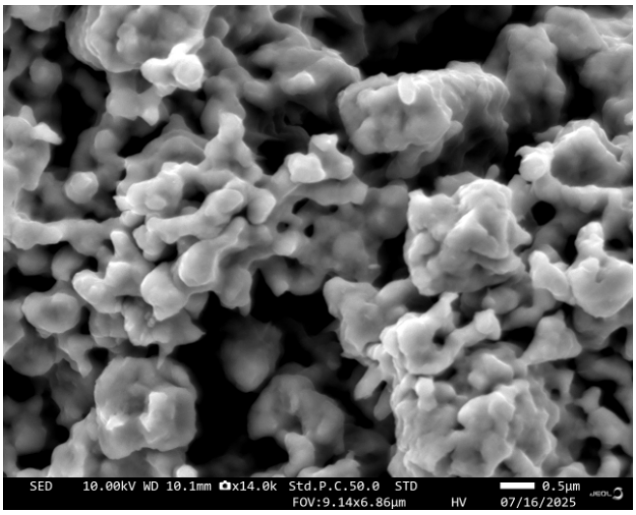

(b) 300 °C–1 h, 14k

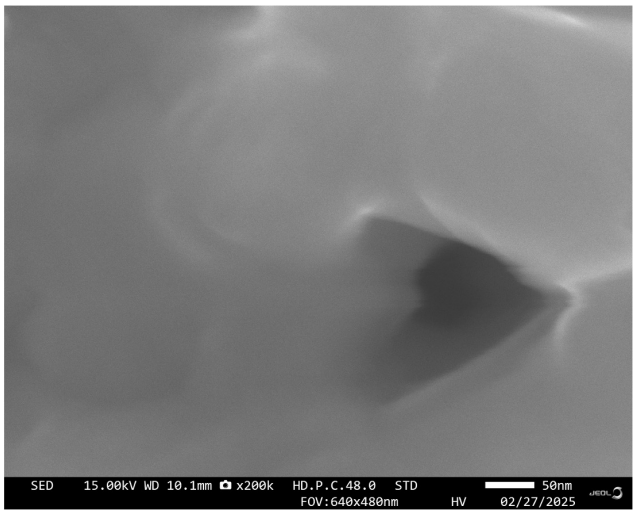

(c) 300 °C–1 h, 200k

Figure 23: SEM images of 300 °C–1 h at different magnifications.

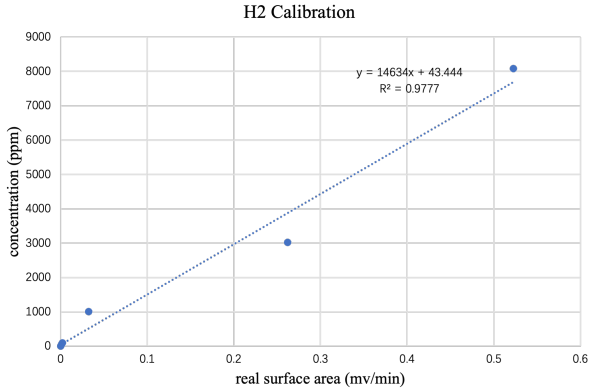

(a) Hydrogen Calibration plot

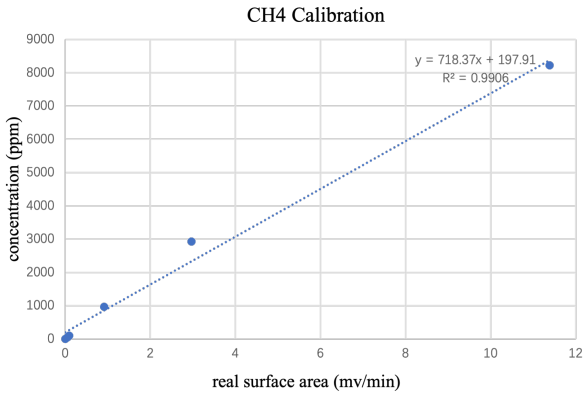

(b) Methane Calibration Plot

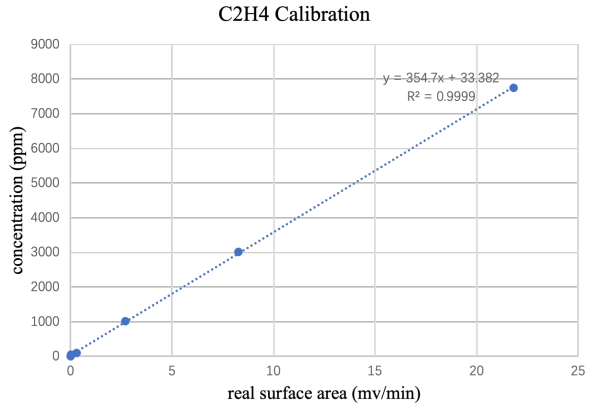

(c) Ethylene Calibration Plot

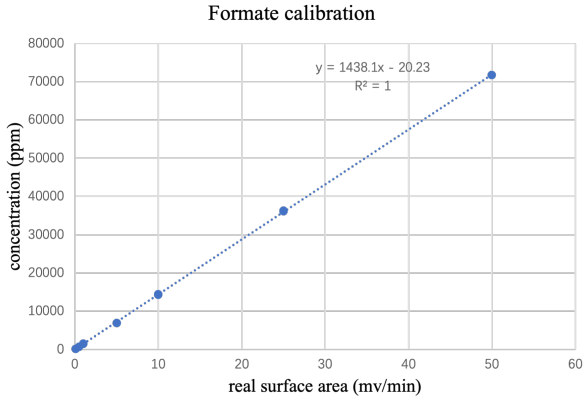

(d) Formate Calibration Plot

Figure 24: Calibration Plots for products in GC and HPLC. Symbols represent real data, while lines indicate calibration data.